Walz W, Ilschner S, Ohlemeyer C, Banati R, Kettenmann H. 1993. Extracellular ATP activates a cation conductance and a K^+ conductance in cultured microglial cells from mouse brain. J Neurosci 13:4403–4411.

Webb SE, Pollard JW, Jones GE. 1996. Direct observation and quantification of macrophage chemoattraction to the growth factor CSF-1. J Cell Sci 109:793–803.

Weiss-Haljiti C, Pasquali C, Ji H, Gillieron C, Chabert C, Curchod ML, Hirsch E, Ridley AJ, van Huijsduijnen RH, Camps M, Rommel C. 2004. Involvement of phosphoinositides 3-kinase γ, Rac, and PAK signaling in chemokine-induced macrophage migration. J Biol Chem 279:43273–43284.

Xiang Z, Burnstock G. 2005. Expression of P2X receptors on rat microglial cells during early development. Glia 52:119–126.

Yano S, Tokumitsu H, Soderling TR. 1998. Calcium promotes cell survival through CaM-K kinase activation of the protein-kinase-B pathway. Nature 396:584–587.

Yogosawa S, Hatakeyama S, Nakayama KI, Miyoshi H, Kohsaka S, Akazawa C. 2005. Ubiquitylation and degradation of serum-inducible kinase by hVPS18, a RING-H2 type ubiquitin ligase. J Biol Chem 280: 41619–41627.

Zhang Z, Artelt M, Burnet M, Trautmann K, Schluesener HJ. 2006. Lesional accumulation of $P2X_4$ receptor monocytes following experimental traumatic brain injury. Exp Neurol 197:252–257.

THE JOURNAL OF COMPARATIVE NEUROLOGY 483:329–340 (2005)

Neuronal Generation, Migration, and Differentiation in the Mouse Hippocampal Primoridium as Revealed by Enhanced Green Fluorescent Protein Gene Transfer by Means of In Utero Electroporation

EIKO NAKAHIRA* AND SHIGEKI YUASA
Department of Ultrastructural Research, National Institute of Neuroscience, National Center of Neurology and Psychiatry, Kodaira, Tokyo 187-8502, Japan

ABSTRACT

Neuronal migration defects in the hippocampus during development are thought to be involved in various mental disorders. Studies of neural cell migration in the developing cerebrum have focused mainly on the neocortex, but those that have been performed on the developing hippocampal formation have not been adequately carried out. In the present study, the morphological differentiation of immature neurons that form the laminar structure of the hippocampus was investigated by labeling ventricular surface cells with the expression vector of the enhanced-green-fluorescent-protein (EGFP) gene. Vector DNA was transfected into spatially and temporally restricted neuroepithelium of the hippocampal primordium by in utero electroporation, and the morphology of EGFP-labeled migratory neurons and their interrelationships with the radial glial arrangement were observed. Pyramidal cells of Ammon's horn began to migrate radially along glial processes from a broad area of neuroepithelium on embryonic day (E)14. Large numbers of multipolar cells were found in the intermediate zone in the initial stage and stratified pyramidal cells appeared later. Dentate granule cells were labeled later than (E)16 and originated from a restricted area of neuroepithelium adjacent to the fimbria. Their initial migration was rapid and independent of radial glial fibers. Subsequent tangential migration in the subpial space and their ultimate settling into the forming dentate gyrus were closely associated with the radial glia. These findings indicate that distinct cellular mechanisms are involved in the development of the cortical layer of Ammon's horn and dentate gyrus. J. Comp. Neurol. 483:329–340, 2005.

Indexing terms: development; pyramidal cell; granule cell; radial glia

The hippocampus contains the neural circuitry that is crucial for higher brain functions, such as learning, memory, and affect. Many pathological conditions, such as epilepsy (Houser, 1990; Lurton et al., 1997; Haas et al., 2002), lissencephaly (Sato et al., 2001; Ross et al., 2001), Down's syndrome (Raz et al., 1995), and psychiatric disorders (Benes and Berretta, 2001; Connor et al., 2004) are associated with histological abnormalities in the hippocampus, and the abnormalities are likely to be related to a disruption of neuronal migration during development. Thus, knowledge of neuronal migration during hippocampal histogenesis is necessary to be able to analyze the pathogenesis of the above conditions.

The development of cortical structures in the mammalian brain is achieved by a combination of two types of

Grant sponsor: Ministry of Health, Labor and Welfare, Japan; Grant number: Research Grant (15B-3) for Nervous and Mental Disorders (to S.Y.).

*Correspondence to: Eiko Nakahira, Department of Ultrastructural Research, National Institute of Neuroscience, National Center of Neurology and Psychiatry, 4-1-1 Ogawahigashi, Kodaira, Tokyo 187-8502, Japan. E-mail: nakahira@ncnp.go.jp

Received 19 August 2004; Revised 4 November 2004; Accepted 8 November 2004

DOI 10.1002/cne.20441

Published online in Wiley InterScience (www.interscience.wiley.com).

neuronal migration, radial migration from corresponding neuroepithelium and tangential migration of cells of separate other origin. The combination of the two types of neuronal migration elaborates the complex and well-organized cortical structures, such as the cortical structure of the neocortex (Rakic, 1972; Anderson et al., 1997; Marin and Rubenstein, 2003), hippocampus (Altman and Bayer, 1990a–c), cerebellum (Altman and Bayer, 1985; Hatten and Heintz, 1995), and olfactory bulb (Hinds, 1968; Kishi, 1987).

Previous studies of hippocampal development have shown that two separate sites of origin generate the neurons for its two different cortical structures, Ammon's horn and the dentate gyrus, via different migration routes. The pyramidal neurons in CA1-CA3 are generated by an extensive area of neuroepithelium and migrate radially to the Ammon's horn, while dentate granule cells are generated by a narrow area of neuroepithelium adjacent to the fimbria (FI) and migrate tangentially through the subpial area to form the C-shaped cortical structure (Altman and Bayer, 1990a–c; Bagri et al., 2002). The radial glial arrangement in the developing hippocampus has also been investigated as a crucial substrate for neuronal migration (Rickmann et al., 1987), and the cell migration involved in the hippocampal cortical layer formation has been analyzed by a variety of methods, such as Golgi staining (Stensaas, 1967a–e; Nowakowski and Rakic, 1979; Eckenhoff and Rakic, 1984), labeling the nuclei of migrating cells with [^{3}H] thymidine (Stanfield and Cowan, 1979; Nowakowski and Rakic, 1981; Altman and Bayer, 1990a–c; Reznikov, 1991), and retrovirus vector labeling (Bagri et al., 2002). However, the precise morphology of the migratory neurons and their interrelation with the radial glial arrangement are not adequately understood because there was no method of labeling neuronal precursors at specified times and sites and concomitantly visualizing the morphology of the labeled cells.

The in utero electroporation method enables highly efficient locally and temporally defined introduction of a marker gene into ventricular surface cells in order to characterize the morphology of various phases of migration and the phenotype of the migrating cells (Inoue and Krumlauf, 2001; Tabata and Nakajima, 2001; Saito and Nakatsuji, 2001), and it has been successfully applied to the study of neuronal generation and migration during the development of the cerebral neocortex (Tabata and Nakajima, 2001, 2003; Bai et al., 2003; Kawauchi et al., 2003). Neuronal precursor cells on the ventricular surface should be intensely labeled by transfer of the marker gene in the final mitotic period. After electroporation, the embryos continue to develop normally, and it is possible to analyze the subsequent process of development in vivo. In the present study, the morphology of the migratory neurons and their interrelations with the radial glial arrangement in the mouse hippocampal primordium were investigated by labeling the neuronal precursor cells with EGFP-expression vector at specified stages of development.

Abbreviations

AH	Ammon's horn
CP	cortical plate
DG	dentate gyrus
DGE	external limb of dentate gyrus
DGI	internal limb of dentate gyrus
DGM	dentate migration
FI	fimbria
HP	hippocampal plate
IMZ	intermediate zone
LV	lateral ventricle
MZ	marginal zone
NC	neocortex
PS	pial surface
SVZ	subventricular zone
VZ	ventricular zone

MATERIALS AND METHODS

Animals

ICR strain mice were purchased from CLEA Japan (Tokyo, Japan). The day of confirmation of vaginal plug was defined as embryonic day zero (E0), and the day of birth was defined as postnatal day zero (P0). At least five animals were used in each experiment. All animal experiments were conducted according to the *Guide for Care and Use of Laboratory Animals* (1996, National Academy of Sciences, USA). All procedures in the animal experiments in this study were approved by the Animal Care Committee of the National Institute of Neuroscience, National Center of Neurology and Psychiatry.

Plasmids

Expression vector pCX-EGFP (Niwa et al., 1991), which contains EGFP cDNA under the control of the CMV enhancer and chick β-actin promoter, was provided by Dr. J. Miyazaki (Division of Stem Cell Regulation Research, Osaka University Medical School, Osaka, Japan).

In utero DNA transfer by electroporation

Plasmid DNA was purified with a CONCERT plasmid maxi kit (Invitrogen, Carlsbad, CA) and dissolved in 1 mM Tris-HCl and 0.1 mM EDTA (pH 8.0) to a concentration of 3–4 μg/μl. The DNA solution also contained 0.05% Fast Green to monitor the injection. Pregnant mice were deeply anesthetized by intraperitoneal injection of sodium pentobarbital (Nembutal, 50 mg/kg body weight, Dainippon Pharmaceutical, Osaka, Japan). The uterine horns were exposed and ~2–4 μl of DNA solution was injected through the uterus into the lateral ventricle of the embryonic forebrain with a glass micropipette (type G-1, Narishige, Tokyo, Japan). After the injection the embryo in the uterus was placed between the electrodes of an electroporator (CUY21, NEPA GENE, Chiba, Japan), and six 50-msec pulses of 35–38 volts were delivered at 75-msec intervals. The uterus was placed back into the abdominal cavity to allow embryonic development to continue. When pCX-EGFP was transfected at E14, and the examination was carried out at E16, this set of conditions was recorded as EGFP/E14:E16 in this study.

Observation of EGFP labeling and immunostaining

The pregnant mice were deeply anesthetized by intraperitoneal injection of sodium pentobarbital and the embryos were removed by cesarean section. The embryos were fixed by transcardiac perfusion with 4% paraformaldehyde (PFA) dissolved in 0.1 M sodium phosphate buffer (PB, pH 7.4), and postfixed overnight at 4°C with the same fixative. Brains were dissected out, embedded in 3% agar in phosphate-buffered saline (PBS), and sliced coronally

with a Microslicer (DTK-3000, DOSAKA EM, Kyoto, Japan) into 200-μm sections. The sections were coverslipped with 80% glycerol and fluorescence images were obtained directly with a confocal laser-scanning microscope (LSM5 Pascal, Zeiss, Oberkochen, Germany).

For immunostaining, the free-floating sections were incubated with the following primary antibodies: mouse anti-MAP-2 monoclonal antibody (HM-2, 1:2,000 dilution, Sigma, St. Louis, MO), mouse anti-neuronal class III β-tubulin monoclonal antibody (TuJ1, 1:2,000 dilution, COVANCE, Berkeley, CA), rabbit anti-glial fibrillary acidic protein (GFAP) polyclonal antibody (1:500 dilution, DAKO, Glostrup, Denmark), mouse anti-nestin monoclonal antibody (Rat-401; Hockfield and McKay, 1985; 1:200 dilution, Developmental Studies Hybridoma Bank, Iowa City, IA). Alexa Fluor-labeled secondary antibodies (1:500 dilution, Molecular Probes, Eugene, OR) were used to detect antigen localization. For double immunostaining for NeuroD and green fluorescent protein (GFP), the sections were treated with 2N-HCl in 0.9% NaCl at room temperature for 1 hour and then washed with PBS five times. Next, the sections were incubated at 4°C overnight with goat polyclonal anti-NeuroD (N-19, 1:200 dilution, Santa Cruz Biotechnology, Santa Cruz, CA) and rabbit polyclonal anti-GFP (1:200 dilution, Molecular Probes). After rinsing with PBS, the sections were incubated at room temperature for 2 hours with Alexa 488-conjugated donkey anti-rabbit IgG (1:500 dilution, Molecular Probes) and Alexa 594-conjugated donkey anti-goat IgG (1:500 dilution, Molecular Probes). The stained sections were mounted on glass slides with 80% glycerol and the sections were examined with a confocal laser-scanning microscope (LSM5 Pascal).

Photodocumentation

Z-series of confocal images of the sections were assembled as a single image with the LSM5 software program. All digital files were imported into Adobe PhotoShop 5.5 (San Jose, CA). After adjustment of contrast and brightness, montages of images were constructed.

Cell counts

The number of labeled cells tended to vary widely from animal to animal, probably because of variability in gene transfection efficiency in the ventricular zone (VZ). All EGFP-labeled cells from the VZ to the cortical plate (CP) were counted to obtain the total cell number. At least 200 EGFP-labeled cells per brain were counted as the total cell number. This approach yielded reproducible percentages of labeled multipolar cells and pyramidal neurons in each animal under the same conditions.

RESULTS

Ammonic pyramidal cell migration

Since previous studies by [^{3}H] thymidine labeling had shown that most pyramidal cells in Ammon's horn are generated around E14 (Angevine, 1965), pCX-EGFP was transfected into the neuroepithelium corresponding to Ammon's horn at E14 in the lateromedial direction, as shown in Figure 1a, and the subsequent migration and differentiation of labeled cells were observed. In 2 days, at E16, EGFP-labeled cells were observed in the VZ, subventricular zone (SVZ), and intermediate zone (IMZ) of the

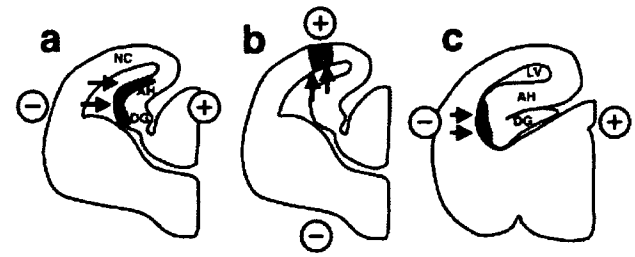

Fig. 1. The relationship between the region of vector transfection by in utero electroporation and the position of the electrodes. The arrows show the direction of the electric current. Plasmid DNA was introduced into the restricted neuroepithelium shown in gray. **a:** The Ammonic neuroepithelium was labeled at E14 in the lateral-to-medial direction. **b:** The neocortical neuroepithelium was labeled at E14 in the ventral-to-dorsal direction. **c:** The primary dentate matrix was labeled at E16 in the lateral-to-medial direction. In all photomicrographs of coronal sections, top is dorsal and left is lateral.

Ammonic primordium (Fig. 2a,e). In the VZ, the cells were elliptic in shape and one end was exposed to the lateral ventricle (Fig. 2e). Most of the labeled cells that had detached from the VZ displayed multipolar morphology with fine processes; that is, had become so-called "multipolar cells" (Tabata and Nakajima, 2003) (Fig. 2e). At E17, some of the multipolar cells in the IMZ had extended processes and had started to differentiate into pyramidal cells (Fig. 2b,f). At E18, spindle-shaped pyramidal cells with branched apical dendrites began to form the incipient CA1 cortical layer, while considerable numbers of multipolar cells remained in the IMZ (Fig. 2c,g). At postnatal day 2 (P2), all the EGFP-labeled cells had long apical dendrites and were aligned in the pyramidal layer, and only small numbers of labeled cells were seen in the VZ (Fig. 2d,h).

To compare corticogenesis in Ammon's horn with corticogenesis in the neocortex, plasmid DNA was introduced into the neocortex in the ventrodorsal direction, as shown in Figure 1b. EGFP/E14:E16 brain is shown in Figure 2i. As reported by Tabata and Nakajima (2003), some of the EGFP-labeled pyramidal cells reached the CP within 2 days after labeling, and large numbers of multipolar cells remained in the SVZ and IMZ (Fig. 2i). In the EGFP/E14:E18 brain, most of the pyramidal cells were aligned in the CP and very few multipolar cells were seen in the SVZ and IMZ (Fig. 2j). By contrast, no EGFP-labeled cells were found within the CP of Ammon's horn at E16 (Fig. 2a,e), and considerable numbers of multipolar cells remained in the SVZ at E18 (Fig. 2g). It took 4 days for Ammonic pyramidal cells to reach the CP (Fig. 2g), in striking contrast to the ~2 days taken for neocortical pyramidal cells to reach the cortex (Fig. 2i).

The percentages of EGFP-labeled cells that were multipolar and pyramidal cells were calculated to analyze the course of morphological differentiation in the CA1 primordium labeled at E14 (Fig. 3). EGFP-positive multipolar cells gradually decreased as a percentage of EGFP-positive cells, and the percentage of EGFP-positive pyramidal cells increased inversely during the period from E16 to P2 (Fig. 3).

To examine the neuronal differentiation of EGFP-labeled cells in Ammon's horn, the hippocampal primordium of EGFP/E14:E18 brain was immunostained with the early-neuron marker TuJ1 or differentiated-neuron

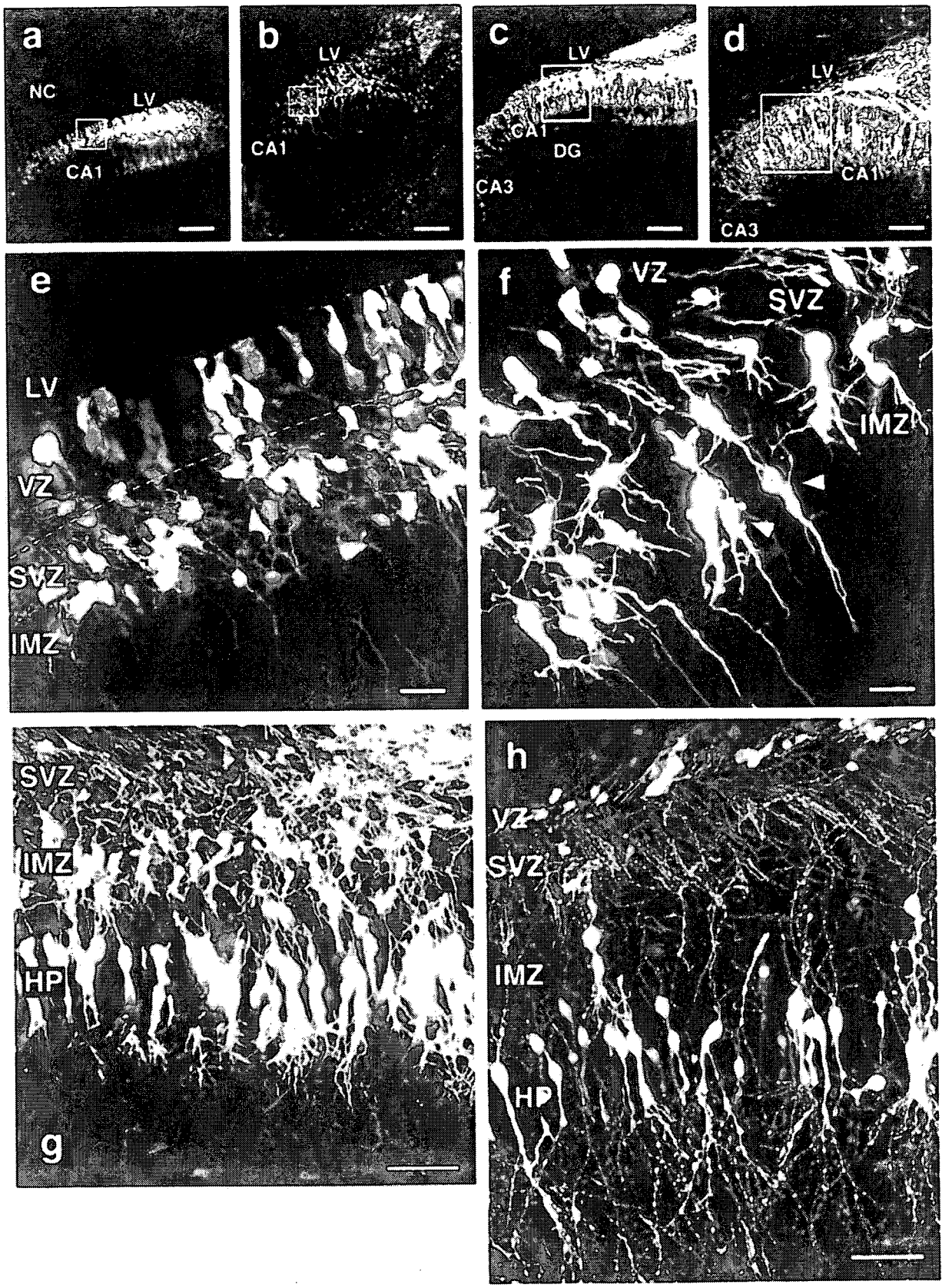

Figure 2 (Continued)

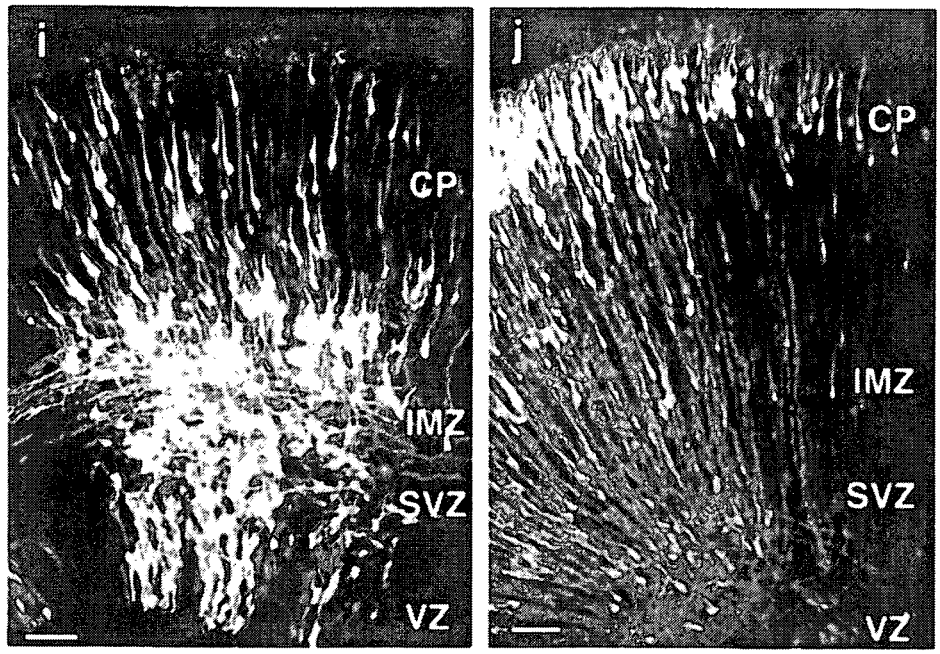

Fig. 2. Migration and differentiation of EGFP-labeled cells in the Ammonic CA1 and neocortical primordia. Coronal sections of the cerebrum transfected with pCX-EGFP at E14. Ammonic primordium (a–h); neocortical primordium (i,j). **a:** EGFP/E14:E16. Most of the EGFP-expressing cells were found in the VZ and SVZ. **b:** EGFP/E14:E17. The labeled cells were found as far as the IMZ. **c:** EGFP/E14:E18. CA1 cortical structure is labeled along with the subcortical layer. **d:** EGFP/E14:P2. Most of the EGFP-labeled cells have settled in the CA1 cortical plate. **e:** Higher magnification of the boxed area in (a). Both the ventricular neuroepithelium and the multipolar cells in the SVZ are labeled. The broken line represents the border between the VZ and SVZ. **f:** Higher magnification of the SVZ and IMZ in the boxed area in (b). Elongated spindle shaped-cells (indicated by arrowheads) have appeared among the multipolar cells in the SVZ and IMZ. **g:** Higher magnification of IMZ and HP in the boxed area in (c). Pyramidal cells are arranged in the HP, while many multipolar cells remain in the IMZ. **h:** Higher magnification of the boxed area in (d). EGFP-labeled pyramidal cells are aligned in the CA1 cortex. **i:** EGFP/E14:E16. Some EGFP-labeled cells have already reached the neocortical plate 2 days after labeling. Multipolar cells are seen in the SVZ and IMZ. **j:** EGFP/E14:E18. Most of the EGFP-labeled cells have reached and became aligned in the neocortical plate. Scale bars = 200 μm in a–d; 20 μm in e,f; 50 μm in g–j.

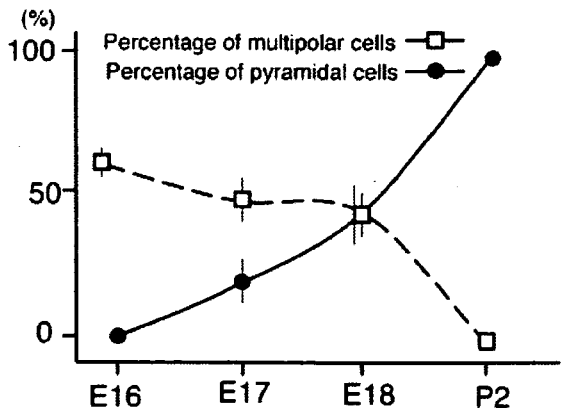

Fig. 3. Multipolar cells and pyramidal cells as a percentage of EGFP-labeled cells during the development of Ammonic CA1 primordium. The vector was transfected at E14 and subsequent changes in each subset as a percentage of all labeled cells were examined. The percentage of multipolar cells (open squares) decreased as the percentage of pyramidal cells (closed circles) increased. The number of cells in each subset is shown as a percentage of all EGFP-labeled cells along the ordinate, and the stage of development is indicated along the abscissa. Each value is a mean ± SEM (n = 4).

marker MAP2. The apical dendrites of EGFP-labeled cells in the densely stratified pyramidal layer were positively immunostained with TuJ1 (Fig. 4a) and MAP2 (Fig. 4b), and the numerous processes of the multipolar cells were also positively immunostained with TuJ1 (Fig. 4c).

To examine the interrelationships between migrating neuronal precursors and radial glial fibers, the hippocampal primordium of EGFP/E14:E16 brain was immunostained with the radial glial marker nestin at E16. Although the processes of the multipolar cell extended independently of the radial fibers, the spindle-shaped cells in the VZ-IMZ were found to be arranged along the radial glial processes (Fig. 4d).

Granule cell migration to the dentate gyrus

Since previous studies have reported that [^{3}H] thymidine uptake by dentate granule cells of the mouse starts to become intense on E16 (Angevine, 1965), the generation and migration of dentate granule cells was investigated by transfecting pCX-EGFP into the embryonic brain in the lateromedial direction at E16, as shown in Figure 1c.

In the EGFP/E16:E18 brain, the migratory stream of the labeled cells was observed from the restricted area of the VZ adjacent to the fimbria (FI), e.g., the primary

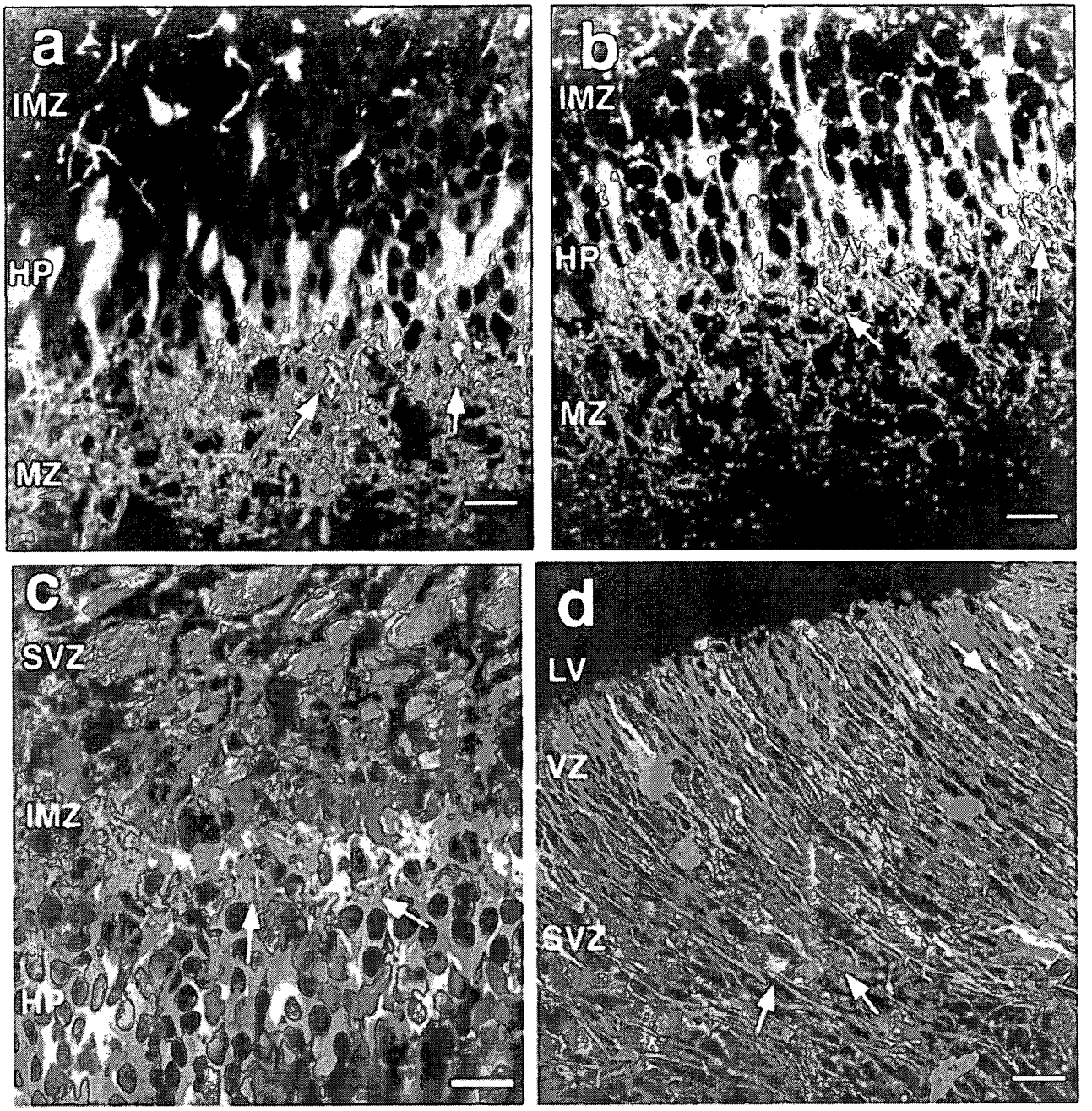

Fig. 4. Neuronal differentiation and neuron-glia interrelation in the Ammonic CA1 primordium. **a:** EGFP/E14:E18. The EGFP-labeled cells are aligned in the HP and exhibit pyramidal-cell morphology, and the neuronal marker TuJ1 (red) is colocalized with the EGFP-positive dendrites (green). **b:** EGFP/E14:E18. MAP2-immunoreactivity (red) is also colocalized with the EGFP-positive dendrites (green) in the pyramidal cells of HP. The arrows in a,b point to TuJ1-positive dendrites and MAP2-positive dendrites, respectively. **c:** EGFP/E14:E18. EGFP-labeled multipolar cells (green) in the IMZ are also immunopositive for TuJ1 (red). The arrows point to TuJ1-positive processes. **d:** EGFP/E14:E16. The EGFP-labeled elongated bipolar cells (green) are arranged along the nestin-immunopositive radial fibers (red). By contrast, the processes of the EGFP-labeled multipolar cell show little association with radial glial processes. The arrows point to elongated bipolar cells. Scale bars = 20 μm.

dentate matrix (Altman and Bayer, 1990c), and labeled cells were found on the migratory route through the subpial space (Fig. 5a). They migrated a long distance. The front of the stream had reached the vicinity of the dentate gyrus at E18, but the labeled cells had not yet stratified (Fig. 5a). At this stage, Ammonic neuroepithelium was also labeled, but there were very few radially migrating cells from VZ to the cortex. Most of the labeled somata

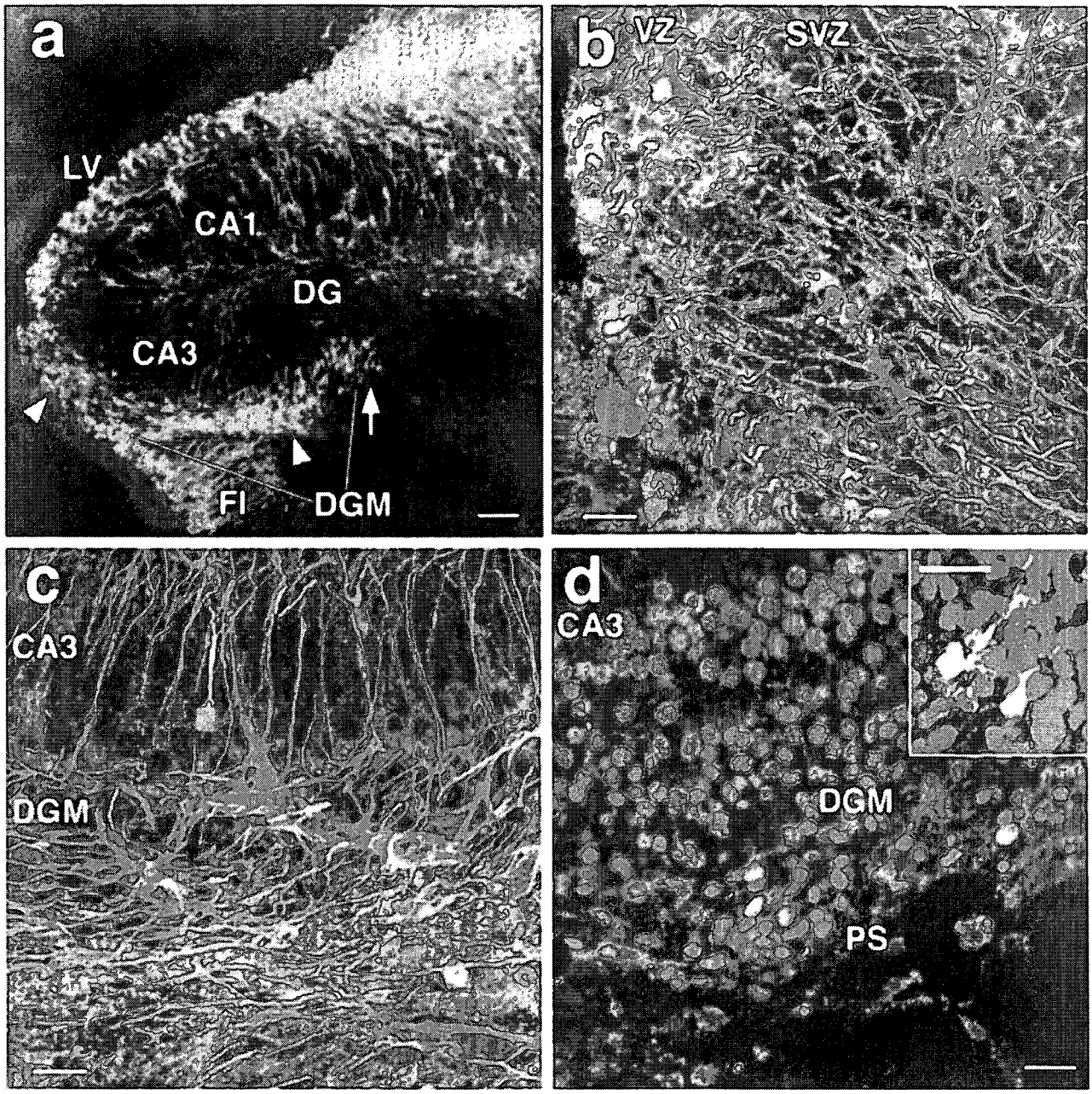

Fig. 5. Migration and differentiation of the granule cell precursors of the dentate gyrus. EGFP/E16:E18 brains were examined histologically. **a:** The stream of EGFP-labeled cells towards the dentate gyrus originated in the primary dentate matrix. The arrow indicates the front of the stream of migrating cells. **b:** Higher magnification of the primary dentate matrix corresponding to the region indicated by the white arrowhead in (a). In the VZ and SVZ, there was little association between the EGFP-labeled cells (green) and nestin-positive radial glial processes (red). **c:** Higher magnification of the subpial stream corresponding to the region indicated by the yellow arrowhead in (a). EGFP-labeled migrating cells (green) are oriented along the tangentially arranged nestin-positive fibers (red). **d:** Double labeling of the subpial migratory stream with anti-EGFP antibody (green) and anti-NeuroD antibody (red). The nuclei of most of the EGFP-positive cells in the subpial migration were immunoreactive for NeuroD. They extended many processes as seen in the projection view of the confocal image in the inset. Scale bars = 100 μm in a; 20 μm in b–d, inset.

were found in the VZ and had extended long radial processes (Fig. 5a). By 5–6 days later (P1–2), dentate migration (DGM) had become stratified in the dentate gyrus (Fig. 6a).

The characteristics of dentate granule cell migration were examined at each step along the path of migration. In the initial stage of migration, most of the labeled cells destined to form the dentate gyrus rapidly detached from

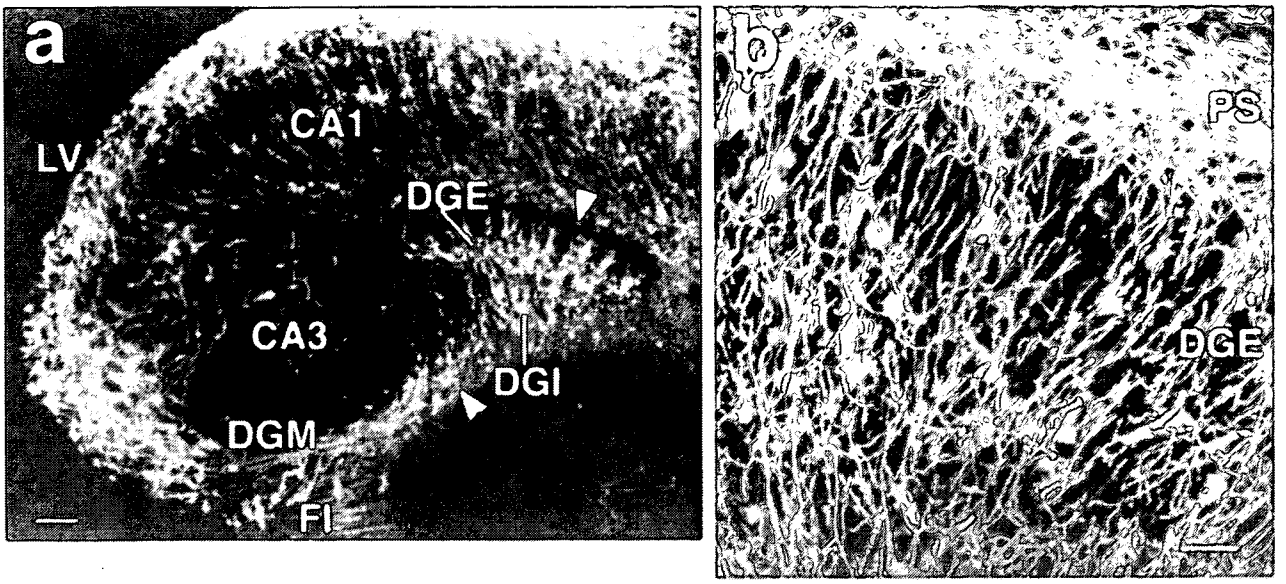

Fig. 6. Granule cell migration and stratification in the dentate gyrus. The EGFP/E16:P2 sections were analyzed. **a:** The migratory stream of EGFP-labeled cells in the subpial region is still evident (yellow arrowhead), and a large number of labeled cells have begun to stratify in the DGE (white arrowhead). **b:** Higher magnification of the DGE indicated by the white arrowhead in (a). EGFP-labeled granule cells (green) migrating towards the dentate cortex are arranged radially and are closely associated with the GFAP-positive radial fibers (red). Scale bars = 100 μm in a; 20 μm in b.

the VZ and SVZ (Fig. 5a,b). They then entered into the tangentially migrating stream in the subpial space and they extended many processes (Fig. 5c,d). To examine the relationship between the migrating granule cells and radial glial fibers, the hippocampal primordium of EGFP/E16:E18 brain was immunostained with an anti-nestin antibody, a marker for radial glia. The arrangement of the glial processes in the VZ of the primary dentate matrix was not radial, and few of the glial process extended in the same direction as the path of the initial cell migration (Fig. 5b).

In the dentate-granule-cell subpial migration stage at E18, the stream was composed of EGFP-labeled cells, and its front had reached the forming dentate gyrus (Fig. 5a). The tangentially migrating cells entering the subpial area had fewer processes and formed a compact stream (Fig. 5c). At the entrance to the subpial region, the EGFP-labeled migratory cells were apposed to tangentially arranged glial processes that were immunopositive for nestin (Fig. 5c). Since NeuroD has been reported to be expressed in immature granule cells (Miyata et al., 1999; Pleasure et al., 2000), double immunostaining with anti-GFP antibody and anti-NeuroD antibody was performed to identify the tangentially migrating cells as immature granule cells. Most of the tangentially migrating EGFP-labeled cells were positive for NeuroD (Fig. 5d), and the tangentially migrating cells that were positive for EGFP and NeuroD had many thin processes (Fig. 5d, inset). Although we also performed immunostaining for NeuN and calretinin, which are also markers of differentiated granule cells, only a few migrating cells in the subpial area were positive at E18 (data not shown).

In the final stage of dentate granule cell migration, EGFP-labeled cells reached dentate gyrus in 5 days and became arranged in the cortical layer in EGFP/E16:P2 brain (Fig. 6a,b). Some of the labeled cells were still migrating tangentially in the subpial space (Fig. 6a). The relationship between the EGFP-labeled granule cells and radial fibers was investigated by immunostaining the dentate gyrus of EGFP/E16:P2 brain with anti-GFAP antibody as a marker of late-stage radial glia, and the result showed that the EGFP-labeled unipolar cells in the external limb of the dentate gyrus (DGE) were radially arranged in close apposition to the radial processes of the dentate unipolar astroglia (Fig. 6b).

Cell migration to CA3

Since adult CA3 neurons of the mouse were labeled when [^{3}H] thymidine was injected around E14 (Angevine, 1965), cell migration to the CA3 was studied by introducing the EGFP-expression vector into the hippocampal primordium at E14 in the lateromedial direction (Fig. 1a), and the embryos were dissected at E18. A large number of EGFP-labeled cells were found in the neuroepithelium between the CA1 primordium and the fimbria (FI) (Fig. 7a), and most of the cells migrating to the CA3 region exhibited multipolar morphology (Fig. 7b). Some of the CA3-forming cells had originated elsewhere. Examination of EGFP/E16:E18 brain showed that most of the EGFP-labeled cells had migrated tangentially in the subpial space (Fig. 7c), but that a small proportion of labeled cells with a single process had detached from the compact stream (Fig. 7c,d) and migrated along the radially arranged nestin-positive glial processes oriented toward CA3 (Fig. 7d).

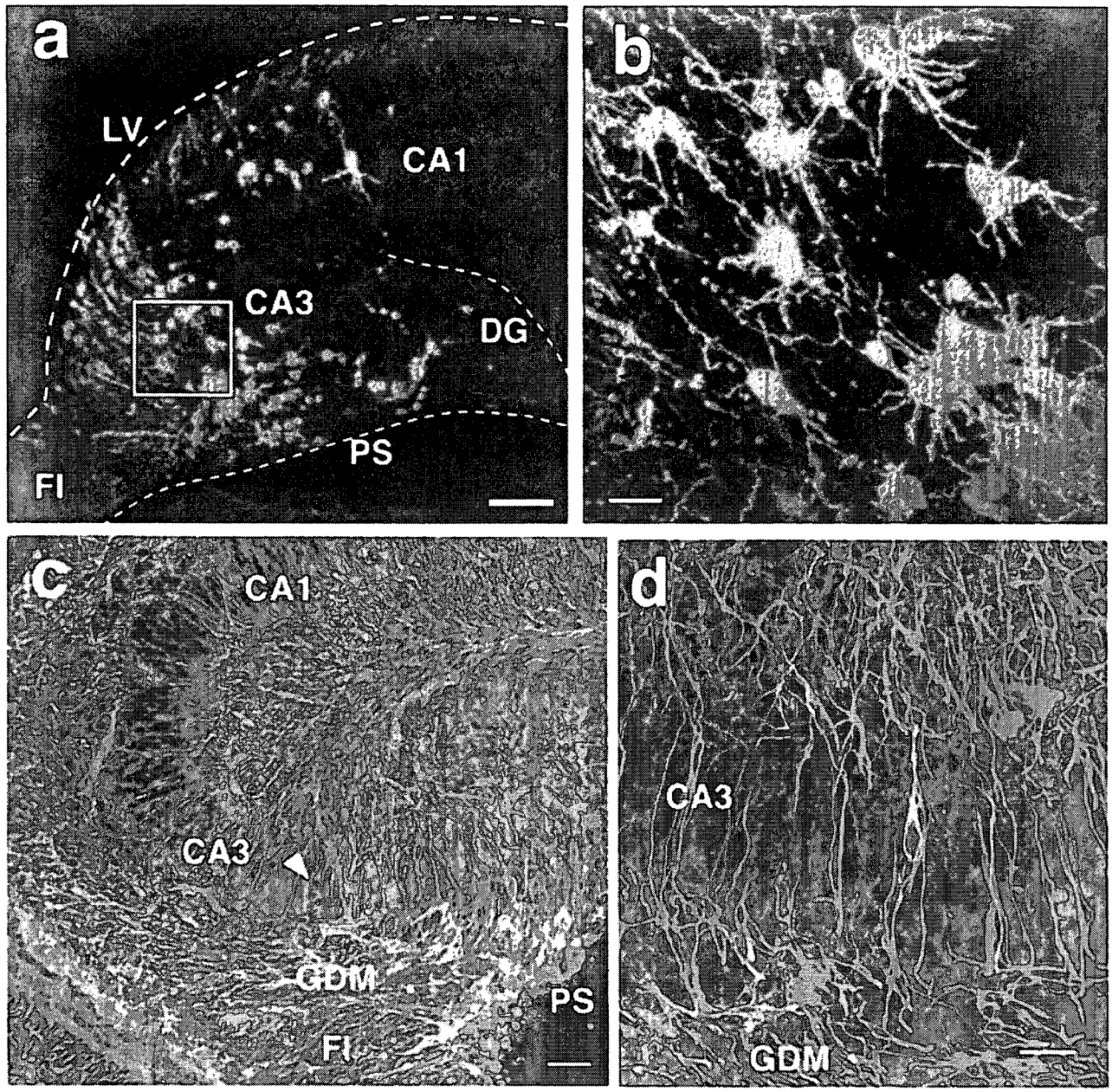

Fig. 7. Neuronal migration to the CA3. **a:** EGFP/E14:E18. Large numbers of EGFP-labeled cells were distributed from the VZ to the forming CA3. **b:** Higher magnification of the boxed area in (a). The labeled cells exhibit multipolar cell morphology. **c:** EGFP/E16:E18. The section was immunostained with anti-nestin antibody. EGFP-labeled cells (green) are seen arranged along the nestin-immunopositive radial processes (red) in the CA3 cortical plate. Small numbers of EGFP-labeled cells are migrating radially towards the CA3 (arrowhead) from a large stream of EGFP-labeled cells tangentially migrating in the subpial region. **d:** Higher magnification of the region indicated by the arrowhead in (c). EGFP-labeled unipolar cells are closely associated with nestin-positive radial fibers. Scale bars = 100 μm in a; 20 μm in b,d; 50 μm in c.

DISCUSSION

The results of this study demonstrate the morphological basis of the migration and differentiation of hippocampal neurons during corticogenesis, as summarized in Figure 8. The neuronal precursors of Ammonic pyramidal cells and dentate granule cells were labeled with EGFP-expression vector at specified developmental stages. The formation of each cortical structure consisted of multistep mechanisms of migration and differentiation and different neuron-glia interrelationships. To our knowledge, this is the first report of a study in which hippocampal migratory neurons were morphologically analyzed by foreign gene transfer by means of in utero electroporation.

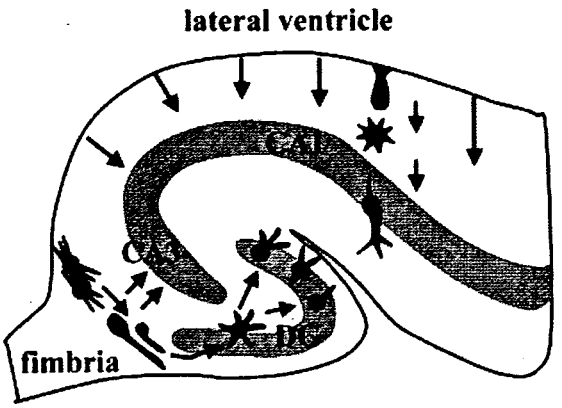

Fig. 8. Diagram summarizing the neuronal migration in the hippocampal primordium demonstrated in the present study. The pyramidal cells of CA1 and CA3 arose from an extensive area of neuroepithelium at E14 and changed the morphology during radial migration, as shown in the CA1 region. Dentate granule cells arose from the restricted VZ adjacent to the fimbria, migrated tangentially in the subpial area, and stratified in the dentate gyrus; their morphology also changed during migration. Some of the tangentially migrating cells changed their route and migrated toward CA3.

Migration and differentiation of pyramidal cells in the development of cortical structure of CA1

Previous studies by [^{3}H] thymidine labeling demonstrated the prolonged sojourn of immature pyramidal neurons along the migratory pathway towards the Ammonic cortex in the rat (Altman and Bayer, 1990b), and it took 4 days for the migratory pyramidal cells to reach the Ammonic cortical plate after the final mitosis in the VZ. Similar results were obtained in the mouse Ammonic primordium when the pyramidal cell precursors were labeled with EGFP-expression vector at E14 in the present study. The labeled neurons reached the Ammonic plate at E18 and exhibited the morphology of differentiated pyramidal cells. Since the final mitosis of CA1 pyramidal cells in the mouse occurs during E13–15 (Angevine, 1965), the intensely labeled population should have completed their final mitosis around the time of labeling.

The remarkable finding in the present study was the transient appearance of large numbers of EGFP-labeled multipolar cells in the SVZ and IMZ during E16–18 (Fig. 2e–g). Their morphology has been described in the hippocampal primordium of the rabbit (Stensaas, 1967a,b) and monkey (Nowakowski and Rakic, 1979) by the Golgi method, but their significance has not been adequately discussed. The presence of the multipolar cells in the SVZ and IMZ has also been reported in neocortical development (Noctor et al., 2001, 2004; Tabata and Nakajima, 2003). In our study, the multipolar cells accounted for 30.1% of the EGFP-labeled cells in the neocortical primordium of the mouse at E16 (Fig. 2i). Their migratory pattern within the subcortical zone is nonradial and has been described as "multipolar migration" (Tabata and Nakajima, 2003), as opposed to radial locomotion or somal translocation. The multipolar cells migrate slowly, at about one-fifth the rate of the bipolar cells in the neocortex (Tabata and Nakajima, 2003; also Fig. 2i,j).

The multipolar cells in the hippocampal CA1 primordium displayed morphology very similar to that of the multipolar cells in the neocortical primordium. During E16–18, large numbers of multipolar cells remained in the SVZ and IMZ, and there was little correlation between the processes of those multipolar cells and the radial glia arrangement (Fig. 4d), suggesting nonradial migration, the same as in the neocortex. By contrast, at E16 small numbers of elongated bipolar cells were found in the subcortical zone and were arranged in parallel with nestin-immunopositive radial glial processes (Fig. 4d). The number of multipolar cells had decreased significantly by E18, and they had disappeared by P2. During the same period, pyramidal cells appeared and increased in the Ammonic plate of CA1 (Fig. 3). These findings suggest that multipolar cells transdifferentiate into pyramidal neurons during migration to the Ammonic plate, the same as in the neocortex (Noctor et al., 2004).

The average migration rate of the pyramidal precursors during CA1 development (4–5 days) was much slower than that during neocortical development (1–2 days). In the hippocampal primordium, multipolar cells make up most of the population of subcortical precursors of the Ammonic plate (57.1 ± 3.3%; Fig. 3). The prolonged sojourn of pyramidal cells is thought to at least partly be due to their differentiation through the slowly migrating multipolar cells. The molecular basis that underlies the difference in migratory rate between bipolar cells and multipolar cells is not known at present. Reelin, a large extracellular protein that controls neuronal migration (D'Arcangelo et al., 1995; Gilmore and Herrup, 2000; Rice and Curran, 2001; Luque et al., 2003) and exhibits an inhibitory action on the radial migration of cortical neurons (Dulabon et al., 2000), may be one of the molecules responsible for the retention of CA1 neurons. Since the number of Cajal-Retzius cells secreting Reelin in the marginal zone is significantly larger in the hippocampus than in the neocortex (Soriano et al., 1994), the higher production of Reelin (Nakajima et al., 1997; Alcantara et al., 1998) may diminish the migratory speed of CA1 neurons to a larger extent than the migratory speed of neocortical neurons. The retention of CA1 neurons may be significant in terms of the specification of axonal patterns. The later growth of afferent axons into the hippocampal primordium at E17–18 (Super and Soriano, 1994; Soriano et al., 1994) is well coordinated with the late stratification and dendrite growth of their target CA1 pyramidal neurons. The finding that afferent fiber segregation in the CA1 depends on the position of the postsynaptic target neurons supports the above idea (Deller et al., 1999).

Granule cell migration and differentiation

The granule cells generated by the dentate neuroepithelium (primary dentate matrix) in the embryonic stage are thought to migrate out and form the secondary dentate matrix as they migrate tangentially. The tertiary dentate matrix subsequently forms the deep layer of the dentate gyrus, and neurogenesis continues to adulthood in the hilus (Altman and Bayer, 1990c). Although dentate granule cells continue to proliferate in adulthood, heavy labeling of dentate granule cells in the adult hippocampus can be obtained by [^{3}H] thymidine administration from E16 onward in the mouse (Angevine, 1965). These previous findings indicate that a large portion of dentate granule cells complete their final mitosis at sites ranging from the primary dentate matrix to the tertiary matrix on E16 or thereafter. In the present study, labeling of migratory

granule cells by the transfection of EGFP-expression vector into the VZ was also possible on E16 onward. Labeling the VZ on E16 should have labeled a cohort of granule cells that completed their final mitosis just around the time of transfection. A previous study demonstrated that the granule cells generated during the prenatal period form the outside shell of the granular layer in an outside-in pattern (Altman and Bayer, 1990c), a finding that is highly consistent with the finding in our own study that only the outer layer of the dentate gyrus was labeled by transfection of EGFP-expression vector at E16 (Fig. 6a,b).

Little information has ever been obtained about the morphology of the granule cells that migrate to the dentate gyrus, especially in the embryonic stage. The EGFP labeling by in utero electroporation allowed at least a subset of the granule cells generated in the prenatal period to be morphologically analyzed. The process of migration observed in the present study could be divided into three steps: 1) initial migration from the primary dentate matrix, 2) subpial migration through the secondary dentate matrix, and 3) stratification into the cortical structure of the dentate gyrus.

In the primary dentate matrix, labeled immature granule cells detach from the VZ and migrate without apparent guidance by glial processes (Fig. 5b). These immature neurons extend many short processes in various directions. When they enter the subpial migratory stream, they display various morphologies, including bipolar cell (Fig. 5c) and multipolar cell morphology (Fig. 5d). Since NeuroD has been reported to be expressed in the dentate granule cells as early as the stage of detachment from the VZ (Pleasure et al., 2000), the subpial cells double-labeled by EGFP and NeuroD were considered to exhibit the morphology of migratory granule cells. The entire subpial stream of dentate granule cells followed the nestin-positive glial processes, which extend tangentially in the subpial space.

In the final stage of granule cell migration to the dentate gyrus, the arrangement of the EGFP-labeled granule cells was closely correlated with arrangement of the radial glial processes in the forming cortical structure of the dentate gyrus, especially in the outer cortical region (Fig. 6b). The migration of dentate granule cells was directed outward toward the pia mater, in contrast to the inward migration of cerebellar granule cells along the radial processes of Bergmann glia (Rakic, 1971; Komuro and Rakic, 1998). Thus, the final step of granule cell migration in the hippocampal dentate gyrus and cerebellar cortex is morphologically similar and the similarity is also corroborated by the morphological similarity between the unipolar astroglia in the dentate gyrus and the Bergmann glia in the cerebellum (Edwards et al., 1990). Moreover, the observation on guided migration of dentate granule cells along Bergmann glial processes in a culture system also suggested the involvement of common molecular mechanisms in cortical formation by cerebellar and dentate granule cells (Gasser and Hatten, 1990a,b).

Mutations in the genes involved in the Reelin signaling pathway (Stanfield and Cowan, 1979; Sheldon et al., 1997; Trommsdorf et al., 1999) induce the malformation of the unipolar astrocytes and disarrangement of granule cells in the dentate gyrus (Frotscher et al., 2003; Weiss et al., 2003). However, subpial migration is not very severely impaired, because it follows glial fibers but may not be very dependent on glial guidance. These findings are consistent with the different neuron-radial glia interrelations during granule cell migration observed in the present study.

Development of CA3 cortical structure

CA3 pyramidal neurons in the mouse have been reported to be generated during the E13–15 period, the same as CA1 neurons (Angevine, 1965). In the present study, a subset of migratory cells labeled with EGFP at E14 was found to originate from the neuroepithelium between CA1 and the dentate primordium, and a large proportion of the cells that migrated to CA3 also exhibited the morphology of multipolar cells in the SVZ and IMZ (Fig. 7b). The basic mechanism of CA3 corticogenesis is therefore thought to be similar to the mechanism in CA1.

However, a remarkable finding in CA3 corticogenesis was that another migratory stream that was labeled later, at E16, was also directed into CA3 during the period of dentate granule cell migration (Fig. 7c). Small numbers of EGFP-labeled cells detached from the migratory stream in the subpial area and migrated into the cortical layer of CA3 along the radial glia, which were arranged perpendicular to the subpial glial processes (Fig. 7d). These cells migrating into CA3 are thought to belong to the late-generated subpopulation of precursors of CA3 neurons.

The significance of the migratory population from the subpial stream to CA3 is unknown. The formation of CA3 is delayed, consistent with the delayed formation of the dentate gyrus (Altman and Bayer, 1990b), and the development of the mossy fiber projection from the dentate gyrus to CA3 may also be temporally coordinated in the neonatal stage to form the main intrahippocampal circuit (Gaarskjaer, 1985). It is tempting to think that the late-generated CA3 neurons migrate along the migratory route of the granule cells by using the same guiding cues.

LITERATURE CITED

Alcantara S, Ruiz M, D'Arcangelo G, Ezan F, de Lecea L, Curran T, Sotelo C, Soriano E. 1998. Regional and cellular patterns of reelin mRNA expression in the forebrain of the developing and adult mouse. J Neurosci 18:7779–7799.

Altman J, Bayer SA. 1985. Embryonic development of the rat cerebellum. I. Delineation of the cerebellar primordium and early cell movements. J Comp Neurol 231:1–26.

Altman J, Bayer SA. 1990a. Mosaic organization of the hippocampal neuroepithelium and the multiple germinal sources of dentate granule cells. J Comp Neurol 301:325–342.

Altman J, Bayer SA. 1990b. Prolonged sojourn of developing pyramidal cells in the intermediate zone of the hippocampus and their settling in the stratum pyramidale. J Comp Neurol 301:343–364.

Altman J, Bayer SA. 1990c. Migration and distribution of two populations of hippocampal granule cell precursors during the perinatal and postnatal periods. J Comp Neurol 301:365–381.

Anderson SA, Eisenstat DD, Shi L, Rubenstein JLR. 1997. Interneuron migration from basal forebrain to neocortex: dependence on Dlx genes. Science 278:474–476.

Angevine JB. 1965. Time of neuron origin in the hippocampal region. An autoradiographic study in the mouse. Exp Neurol 2:1–70.

Bagri A, Gurney T, He X, Zou YR, Littman DR, Tessier-Lavigne M, Pleasure SJ. 2002. The chemokine SDF1 regulates migration of dentate granule cells. Development 129:4249–4260.

Bai J, Ramons RL, Ackman JB, Thomas AM, Lee RV, LoTurco JJ. 2003. RNAi reveals doublecortin is required for radial migration in rat neocortex. Nat Neurosci 6:1277–1283.

Benes FM, Berretta S. 2001. GABAergic interneurons: implications for understanding schizophrenia and bipolar disorder. Neuropsychopharmacology 25:1–27.

Connor SE, Ng V, McDonald C, Schulze K, Morgan K, Dazzan P, Murray RM. 2004. A study of hippocampal shape anomaly in schizophrenia and in families multiply affected by schizophrenia or bipolar disorder. Neuroradiology 46:523–534.

D'Arcangelo G, Miao GG, Chen SC, Soares HD, Morgan JI, Curran T. 1995.

A protein related to extracellular matrix proteins deleted in the mouse mutant reeler. Nature 374:719–723.

Deller T, Drakew A, Heimrich B, Forster E, Tielsch A, Frotscher M. 1999. The hippocampus of the reeler mutant mouse: fiber segregation in area CA1 depends on the position of the postsynaptic target cells. Exp Neurol 156:254–267.

Dulabon L, Olson EC, Taglienti MG, Eisenhuth S, McGrath B, Walsh CA, Kreidberg JA, Anton ES. 2000. Reelin binds alpha3beta1 integrin and inhibits neuronal migration. Neuron 27:33–44.

Eckenhoff MF, Rakic P. 1984. Radial organization of the hippocampal dentate gyrus: a Golgi, ultrastructural, and immunocytochemical analysis in the developing rhesus monkey. J Comp Neurol 223:1–21.

Edwards MA, Yamamoto M, Caviness VS Jr. 1990. Organization of radial glia and related cells in the developing murine CNS. An analysis based upon a new monoclonal antibody marker. Neuroscience 36:121–144.

Frotscher M, Haas CA, Forster E. 2003. Reelin controls granule cell migration in the dentate gyrus by acting on the radial glial scaffold. Cereb Cortex 13:634–640.

Gaarskjaer F. 1985. The development of the dentate area and the hippocampal mossy fiber projection of the rat. J Comp Neurol 241:154–170.

Gasser UE, Hatten ME. 1990a. Central nervous system neurons migrate on astroglial fibers from heterotypic brain regions in vitro. Proc Natl Acad Sci U S A 87:4543–4547.

Gasser UE, Hatten ME. 1990b. Neuron-glia interactions of rat hippocampal cells in vitro: glia-guided neuronal migration and neuronal regulation of glial differentiation. J Neurosci 10:1276–1285.

Gilmore EC, Herrup K. 2000. Cortical development: receiving reelin. Curr Biol 10:162–166.

Haas CA, Dudeck O, Kirsch M, Huszka C, Kann G, Pollak S, Zentner J, Frotscher M. 2002. Role for reelin in the development of granule cell dispersion in temporal lobe epilepsy. J Neurosci 22:5797–5802.

Hatten ME, Heintz N. 1995. Mechanisms of neural patterning and specification in the developing cerebellum. Annu Rev Neurosci 18:385–408.

Hinds JW. 1968. Autoradiographic study of histogenesis in the mouse olfactory bulb. II. Cell proliferation and migration. J Comp Neurol 134:305–322.

Hockfield S, McKay RD. 1985. Identification of major cell classes in the developing mammalian nervous system. J Neurosci 5:3310–3328.

Houser CR. 1990. Granule cell dispersion in the dentate gyrus of humans with temporal lobe epilepsy. Brain Res 535:195–204.

Inoue T, Krumlauf R. 2001. An impulse to the brain-using in vivo electroporation. Nat Neurosci 4:1156–1158.

Kawauchi T, Chihama K, Nabeshima Y, Hoshino M. 2003. The in vivo roles of STEF/Tiam1, Rac1 and JNK in cortical neuronal migration. EMBO J 22:4190–4201.

Kishi K. 1987. Golgi studies on the development of granule cells of the rat olfactory bulb with reference to migration in the subependymal layer. J Comp Neurol 258:112–124.

Komuro H, Rakic P. 1998. Distinct modes of neuronal migration in different domains of developing cerebellar cortex. J Neurosci 18:1478–1490.

Luque JM, Morante-Oria J, Fairen A. 2003. Localization of ApoER2, VLDLR and Dab1 in radial glia: groundwork for a new model of reelin action during cortical development. Brain Res Dev Brain Res 140:195–203.

Lurton D, Sundstrom L, Brana C, Bloch B, Rougier A. 1997. Possible mechanisms inducing granule cell dispersion in humans with temporal lobe epilepsy. Epilepsy Res 26:351–361.

Marin O, Rubenstein JLR. 2003. Cell migration in the forebrain. Annu Rev Neurosci 26:441–483.

Miyata T, Maeda T, Lee JE. 1999. NeuroD is required for differentiation of the granule cells in the cerebellum and hippocampus. Genes Dev 13: 1647–1652.

Nakajima K, Mikoshiba K, Miyata T, Kudo C, Ogawa M. 1997. Disruption of hippocampal development in vivo by CR-50 mAb against reelin. Proc Natl Acad Sci U S A 94:8196–8201.

Niwa H, Yamamura K, Miyazaki J. 1991. Efficient selection for high-expression transfectants with a novel eukaryotic vector. Gene 108:193–199.

Noctor SC, Flint AC, Weissman TA, Dammerman RS, Kriegstein AR. 2001. Neurons derived from radial glial cells establish radial units in neocortex. Nature 409:714–720.

Noctor SC, Martinez-Cerdeno V, Ivic L, Kriegstein AR. 2004. Cortical neurons arise in symmetric and asymmetric division zones and migrate through specific phases. Nat Neurosci 7:136–144.

Nowakowski RS, Rakic P. 1979. The mode of migration of neurons to the hippocampus: a Golgi and electron microscopic analysis in foetal rhesus monkey. J Neurocytol 8:697–718.

Nowakowski RS, Rakic P. 1981. The site of origin and route and rate of migration of neurons to the hippocampal region of the rhesus monkey. J Comp Neurol 196:129–154.

Pleasure SJ, Collins AE, Lowenstein DH. 2000. Unique expression patterns of cell fate molecules delineate sequential stages of dentate gyrus development. J Neurosci 20:6095–6105.

Rakic P. 1971. Neuron-glia relationship during granule cell migration in developing cerebellar cortex. A Golgi and electronmicroscopic study in Macacus Rhesus. J Comp Neurol 141:283–312.

Rakic P. 1972. Mode of cell migration to the superficial layers of fetal monkey neocortex. J Comp Neurol 145:61–83.

Raz N, Torres IJ, Briggs SD, Spencer WD, Thornton AE, Loken WJ, Gunning FM, McQuain JD, Driesen NR, Acker JD. 1995. Selective neuroanatomic abnormalities in Down's syndrome and their cognitive correlates: evidence from MRI morphometry. Neurology 45:356–366.

Reznikov KY. 1991. Cell proliferation and cytogenesis in the mouse hippocampus. Adv Anat Embryol Cell Biol 122:19–32.

Rice DS, Curran T. 2001. Role of the reelin signaling pathway in central nervous system development. Annu Rev Neurosci 24:1005–1039.

Rickmann M, Amaral DG, Cowan WM. 1987. Organization of radial glial cells during the development of the rat dentate gyrus. J Comp Neurol 264:449–479.

Ross ME, Swanson K, Dobyns WB. 2001. Lissencephaly with cerebellar hypoplasia (LCH): a heterogeneous group of cortical malformations. Neuropediatrics 32:256–263.

Saito T, Nakatsuji N. 2001. Efficient gene transfer into the embryonic mouse brain using in vivo electroporation. Dev Biol 240:237–246.

Sato N, Hatakeyama S, Shimizu N, Hikima A, Aoki J, Endo K. 2001. MR evaluation of the hippocampus in patients with congenital malformations of the brain. Am J Neuroradiol 22:389–393.

Sheldon M, Rice DS, D'Arcangelo G, Yoneshima H, Nakajima K, Mikoshiba K, Howell BW, Cooper JA, Goldowitz D, Curran T. 1997. Scrambler and yotari disrupt the disabled gene and produce a reeler-like phenotype in mice. Nature 389:730–733.

Soriano E, Del Rio JA, Martinez A, Super H. 1994. Organization of the embryonic and early postnatal murine hippocampus. I. Immunocytochemical characterization of neuronal populations in the subplate and marginal zone. J Comp Neurol 342:571–595.

Stanfield BB, Cowan WM. 1979. The development of the hippocampus and dentate gyrus in normal and reeler mice. J Comp Neurol 185:423–460.

Stensaas LJ. 1967a. The development of hippocampal and dorsolateral pallial regions of the cerebral hemisphere in fetal rabbits. I. Fifteen millimeter stage, spongioblast morphology. J Comp Neurol 129:59–70.

Stensaas LJ. 1967b. The development of hippocampal and dorsolateral pallial regions of the cerebral hemisphere in fetal rabbits. II. Twenty millimeter stage, neuroblast morphology. J Comp Neurol 129:71–84.

Stensaas LJ. 1967c. The development of hippocampal and dorsolateral pallial regions of the cerebral hemisphere in fetal rabbits. III. Twenty-nine millimeter stage, marginal lamina. J Comp Neurol 130:149–162.

Stensaas LJ. 1967d. The development of hippocampal and dorsolateral pallial regions of the cerebral hemisphere in fetal rabbits. IV. Forty-one millimeter stage, intermediate lamina. J Comp Neurol 131:409–422.

Stensaas LJ. 1967e. The development of hippocampal and dorsolateral pallial regions of the cerebral hemisphere in fetal rabbits. V. Sixty millimeter stage, glial cell morphology. J Comp Neurol 131:423–436.

Super H, Soriano E. 1994. The organization of the embryonic and early postnatal murine hippocampus. II. Development of entorhinal, commissural, and septal connections studied with the lipophilic tracer DiI. J Comp Neurol 344:101–120.

Tabata H, Nakajima K. 2001. Efficient in utero gene transfer system to the developing mouse brain using electroporation: visualization of neuronal migration in the developing cortex. Neuroscience 103:865–872.

Tabata H, Nakajima K. 2003. Multipolar migration: the third mode of radial neuronal migration in the developing cerebral cortex. J Neurosci 23:9996–10001.

Trommsdorf M, Gotthardt M, Hiesberger T, Shelton J, Stockinger W, Nimpf J, Hammer RE, Richardson JA, Herz J. 1999. Reeler/Disabled-like disruption of neuronal migration in knockout mice lacking the VLDL receptor and ApoE receptor 2. Cell 97:689–701.

Weiss KH, Johanssen C, Tielsch A, Herz J, Deller T, Frotscher M, Forster E. 2003. Malformation of the radial glial scaffold in the dentate gyrus of reeler mice, scrambler mice, and ApoER2/VLDLR-deficient mice. J Comp Neurol 460:56–65.

Three-dimensional reconstruction of the membrane skeleton at the plasma membrane interface by electron tomography

Nobuhiro Morone,[1,2,3] Takahiro Fujiwara,[4] Kotono Murase,[1] Rinshi S. Kasai,[4] Hiroshi Ike,[1] Shigeki Yuasa,[3] Jiro Usukura,[2] and Akihiro Kusumi[1,4]

[1]Kusumi Membrane Organizer Project, Exploratory Research for Advanced Technology (ERATO), Japan Science and Technology Agency, Nagoya 460-0012, Japan
[2]Department of Cell Biology and Anatomy, Graduate School of Medicine, Nagoya University, Nagoya 466-8550, Japan
[3]Department of Ultrastructural Research, National Institute of Neuroscience, National Center of Neurology and Psychiatry, Tokyo 187-8502, Japan
[4]Membrane Mechanisms Project, International Cooperative Research Project (ICORP), Japan Science and Technology Agency, Institute for Frontier Medical Sciences, Kyoto University, Shougoin, Kyoto 606-8507, Japan

Three-dimensional images of the undercoat structure on the cytoplasmic surface of the upper cell membrane of normal rat kidney fibroblast (NRK) cells and fetal rat skin keratinocytes were reconstructed by electron tomography, with 0.85-nm–thick consecutive sections made ~100 nm from the cytoplasmic surface using rapidly frozen, deeply etched, platinum-replicated plasma membranes. The membrane skeleton (MSK) primarily consists of actin filaments and associated proteins. The MSK covers the entire cytoplasmic surface and is closely linked to clathrin-coated pits and caveolae. The actin filaments that are closely apposed to the cytoplasmic surface of the plasma membrane (within 10.2 nm) are likely to form the boundaries of the membrane compartments responsible for the temporary confinement of membrane molecules, thus partitioning the plasma membrane with regard to their lateral diffusion. The distribution of the MSK mesh size as determined by electron tomography and that of the compartment size as determined from high speed single-particle tracking of phospholipid diffusion agree well in both cell types, supporting the MSK fence and MSK-anchored protein picket models.

Introduction

The portion of the cytoskeleton that is closely associated with the cytoplasmic surface of the plasma membrane is often called the membrane skeleton (MSK; Heuser and Kirschner, 1980; Hirokawa and Heuser, 1981; Bennett, 1990; Luna and Hitt, 1992). The term MSK is useful partly because this part of the cytoskeleton is expected to differ from the bulk cytoskeleton in terms of its structure and protein composition, for its interactions with the plasma membrane in general and with specific molecules in the plasma membrane, and also because it plays important roles in a variety of membrane functions. It is involved in the localization of transmembrane proteins at specific sites in the cell membrane (Bennett and Chen, 2001; Pan et al., 2006) and in endocytosis and exocytosis (Gaidarov et al., 1999; Valentijn et al., 2000) in various cell types. It also provides the plasma membrane with the mechanical strength and resilience to withstand the stress and shear forces from the outside environment, which is well established in the thick cortical actin layers in immune cells (Hartwig and Yin, 1988) and in the spectrin–actin network in red blood cells (Mohandas and Evans, 1994; Discher et al., 1995). Therefore, the MSK works as a part of the plasma membrane as well as a part of the cytoskeleton. It is a truly interfacial structure between the bulk cytoskeleton and the 2D bilayer of the plasma membrane.

Recently, a new function of the MSK has become apparent. It was proposed that a part of the MSK is directly and closely associated with the cytoplasmic surface of the plasma membrane, and this part induces partitioning of the cell membrane with regard to the translational diffusion of membrane molecules based on high speed single-particle tracking data on membrane proteins and lipids (Jacobson et al., 1995; Kusumi et al., 2005). In the short-time regime, these membrane molecules are temporarily confined within the compartments delimited by the MSK mesh, and, in the long-time regime, they undergo macroscopic diffusion by hopping between these compartments (MSK fence model). In the fence model, as a result of the collision of the cytoplasmic domains of transmembrane

Correspondence to Akihiro Kusumi: akusumi@frontier.kyoto-u.ac.jp

Abbreviations used in this paper: CCP, clathrin-coated pit; FRSK, fetal rat skin keratinocyte; MSK, membrane skeleton; NRK, normal rat kidney fibroblast.

The online version of this article contains supplemental material.

© The Rockefeller University Press $8.00
The Journal of Cell Biology, Vol. 174, No. 6, September 11, 2006 851–862
http://www.jcb.org/cgi/doi/10.1083/jcb.200606007

Supplemental Material can be found at:
http://www.jcb.org/cgi/content/full/jcb.200606007/DC1

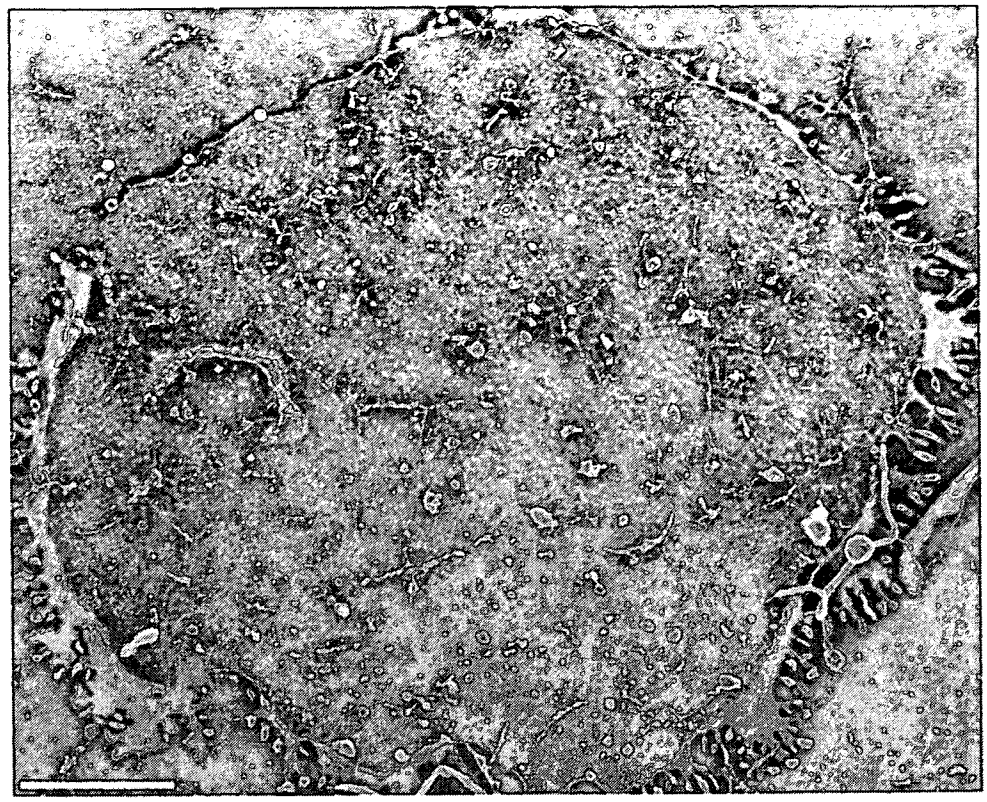

Figure 1. **A bird's-eye view of the large cytoplasmic surface of the upper cell membrane (the membrane facing the buffer rather than the coverslip) of an NRK cell observed by rapid-freeze, deep-etch, freeze-replica EM.** Bar, 2.5 μm.

proteins with the MSK, transmembrane proteins are temporarily confined in the MSK mesh (Sheetz, 1983; Tsuji and Ohnishi, 1986; Tsuji et al., 1988; Saxton, 1989, 1990; Sako and Kusumi, 1994, 1995; Jacobson et al., 1995; Kusumi and Sako, 1996; Saxton and Jacobson, 1997; Sako et al., 1998; Tomishige et al., 1998; Suzuki et al., 2005).

Lipid molecules also undergo hop diffusion, which might be explained by the anchored protein picket model (Fujiwara et al., 2002; Murase et al., 2004; Kusumi et al., 2005). In this model, various transmembrane proteins anchored to the actin-based MSK might effectively act as rows of pickets against the free diffusion of all of the molecules incorporated in the cell membrane as a result of steric hindrance and circumferential slowing (a hydrodynamic frictionlike effect, which propagates quite far from the immobile protein surface; without this effect, pickets will not be effective for blocking diffusion; Bussell et al., 1994, 1995) of the immobile picket proteins anchored to and lined up along the MSK. Lipid movement is affected only by pickets, whereas both pickets and fences would act on transmembrane proteins. These MSK picket-fence effects would be dramatically enhanced when the membrane receptor molecules form signaling complexes upon ligand binding as a result of receptor oligomerization and/or binding of the cytoplasmic signaling molecules to the receptor, leading to the trapping of signaling complexes in the MSK mesh, where the extracellular signal is received. This would enable spatial confinement and regulation of the downstream signaling events (Kusumi and Sako, 1996; Iino et al., 2001).

Despite the importance of the MSK functions and the long history of its study using EM (Byers and Porter, 1977; Heuser and Kirschner, 1980; Hirokawa and Heuser, 1981; Heuser and Anderson, 1989; Hartwig and DeSisto, 1991; Rothberg et al., 1992), our knowledge of its structure and the overall distribution over the plasma membrane has been very limited. For example, we do not know whether the MSK exists everywhere on the cytoplasmic surface of the cell membrane, how extensive the spatial variations of MSK mesh size is, and whether and how MSK interacts with other structures in the plasma membrane such as clathrin-coated pits (CCPs), caveolae, and cell adhesion structures. Even the structure of the MSK of the human red blood cell ghost, a traditional paradigm for MSK studies, is not satisfactorily understood (Sheetz and Sawyer, 1978; Tsukita et al., 1980; Branton et al., 1981; Shen et al., 1986; Ursitti et al., 1991; Takeuchi et al., 1998).

In this study, to further advance our understanding of the MSK structure and function, we observed the undercoat structure on the cytoplasmic surface of the plasma membrane of cultured mammalian cells using rapid-freeze, deep-etch, immunoreplication EM. We paid special attention to the following three points.

First, we tried to consistently prepare and observe large plasma membrane fragments (>10 μm in diameter) to facilitate inspections of very large plasma membrane areas. Almost all of

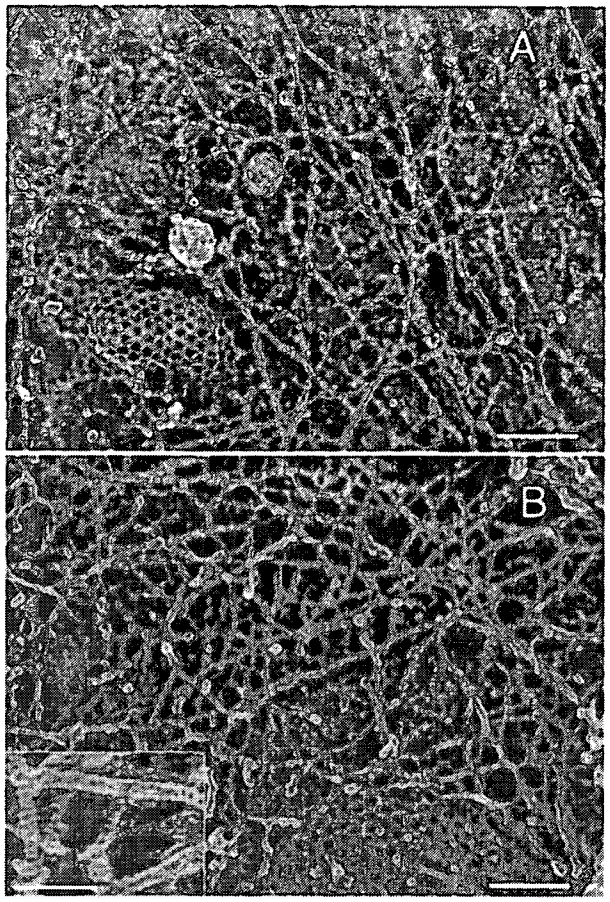

Figure 2. **Magnified MSK images of an NRK and FRSK cell on the cytoplasmic surface of the upper membrane.** (A) NRK cell; (B) FRSK cell. Clathrin-coated structures (A and B) and a caveola (A) show the cytoplasmic surface. The striped banding patterns with the 5.5-nm periodicity on individual filaments are characteristic of actin filaments. These images also reveal close links of the MSK actin filaments with the clathrin-coated structures and caveolae. Bars (A and B), 100 nm; (inset) 50 nm.

the previous MSK studies, including those cited above, investigated the ultrastructural features of the structure of interest, but within a very limited view field. By observing these large membrane surfaces, the spatial variations of the MSK mesh size and of the number density of CCPs and caveolae can be reliably examined.

Second, the 3D reconstruction of the undercoat structure within 100 nm from the cytoplasmic surface of the plasma membrane was performed using electron tomography for the platinum-replicated samples: 97–141 images for a specimen tilted at different angles (every 1°) with respect to the incident electron beam in the range of ±48–70° were obtained and then converted to 100–121 sliced images of every 0.85–1.34 nm for the 3D reconstructed images (Perkins et al., 1997; Medalia et al., 2002; Lucic et al., 2005; McIntosh et al., 2005; Zeuschner et al., 2006).

Third, using the 3D reconstructed images of the MSK structure within 13.6 nm (16 slices of 0.85-nm thickness) from the cytoplasmic surface, the MSK mesh size distribution on the cytoplasmic surface of the plasma membrane was determined. This part of the MSK, which is closely associated with the cytoplasmic surface of the plasma membrane, might form the compartment boundaries for partitioning of the plasma membrane for the diffusion of membrane molecules, thus determining the compartment size. Therefore, it is interesting to compare the distribution of the MSK mesh size on the membrane determined this way and that of the compartment size sensed by membrane molecules. Because the compartment size distributions for membrane molecules are very different between normal rat kidney fibroblast (NRK; median = 230 nm) and fetal rat skin keratinocyte (FRSK; median = 41 nm) cell lines (Fujiwara et al., 2002; Murase et al., 2004), the distribution of the MSK mesh size on the membrane surface was examined using these two cell lines. Although the compartment size is very different between these cell lines, within each cell type, the histogram for the MSK mesh size on the membrane surface is very similar to that for the diffusion compartment size. This strongly supports the MSK fence and MSK-anchored transmembrane protein picket models.

Results

Bird's-eye view of the undercoat structure of the upper cell membrane

Glass coverslips precationized by a treatment with Alcian blue were placed on top of the cells cultured in 35-mm plastic dishes and were allowed to settle and attach to the upper cell membrane at 4°C for 15 min. The buffer containing 1% PFA and 0.25% glutaraldehyde was then added to the space between the coverslip and the plastic bottom of the culture dish. As the coverslip was floated apart, the cells were ruptured and the upper cell membrane was retained, still adhering to the overlaying Alcian blue–coated coverslip. The upper membrane was rapidly frozen by pressing its exposed cytoplasmic surface onto a pure copper block precooled by liquid helium. The frozen sample was deep etched, coated with platinum-carbon, and observed under an electron microscope. We have made extensive efforts to reproducibly prepare and observe large cell membrane fragments >10 μm in diameter.

Fig. 1 is a typical electron micrograph providing a bird's-eye view of the cytoplasmic surface of a large area of the upper cell membrane of a cultured NRK cell. Many such EM images showing the cytoplasmic surfaces of large cell membrane fragments were obtained for NRK and FRSK cells, suggesting that the entire (upper) plasma membrane, except for the places where CCPs and caveolae exist, is coated with the filamentous netlike structure.

Fig. 2 (A and B), which was obtained for an NRK cell (Fig. 2 A) and an FRSK cell (Fig. 2 B), shows the magnified images of the cytoplasmic surface of the plasma membrane, exhibiting extensive filamentous netlike structures, which are the MSK. The presence of clathrin-coated structures shows that this is indeed the cytoplasmic surface. The striped banding patterns with a 5.5-nm periodicity on individual filaments are characteristic of actin filaments and, thus, indicate that these are actin filaments (Heuser and Kirschner, 1980; Heuser, 1983; Katayama,

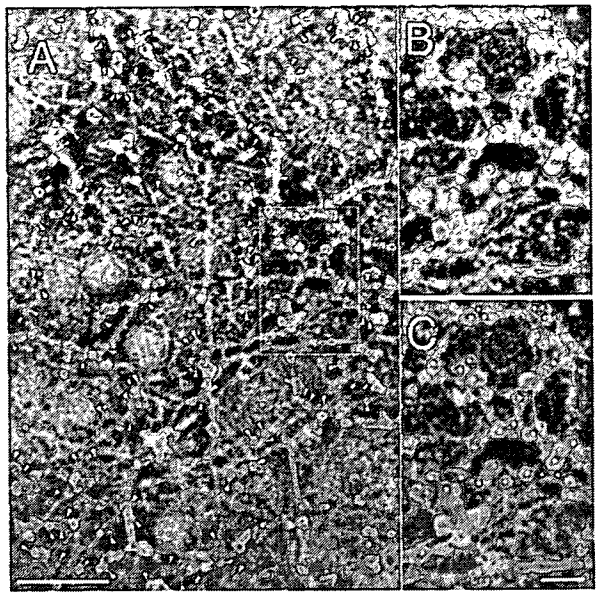

Figure 3. **Immunogold labeling also indicates that the major component of MSK is actin filaments (NRK cell).** Actin filaments were indirectly immunolabeled with 5-nm colloidal gold particles coated with secondary antibodies. Each gold particle can be identified as a clear white spot (colloidal gold particle) surrounded by a fuzzy gray ring, which is caused by the platinum rotary shadowing around the secondary antibody coating of the gold particle. Representative probe images are indicated by arrowheads. (A) Most of the filamentous structures are labeled by colloidal gold probes. (B and C) The boxed area in A is shown at a higher magnification. In C, the gold particles are marked by yellow dots. The filaments with the 5.5-nm striped banding pattern, which is characteristic of the actin filament, are labeled with these gold probes. Bars (A), 200 nm; (B and C) 50 nm.

1998; Schoenenberger et al., 1999). Because almost all of these filaments contain this striped pattern, it is concluded that the MSK is predominantly composed of actin filaments. This was also confirmed by immunogold staining (see Fig. 3 and related text).

The electron micrograph shown in the inset in Fig. 2 B indicates the spatial resolution: because each band in the striped pattern with a 5.5-nm periodicity is visibly separated, the effective resolution is thought to be ~2 nm (both the thickness of the platinum coating and the platinum granule size are ≤2 nm; Heuser and Kirschner, 1980; Heuser, 1983). The MSK structure observed here on the upper cell membrane is similar to that on the bottom cell membrane (the part of the cell membrane facing the coverslip) observed previously (Heuser and Anderson, 1989).

These results suggest that the cytoplasmic surface of a portion of the upper cell membrane >10 μm in diameter was visualized with a spatial resolution of ~2 nm, which is much smaller than the width of a single actin filament or the repeat distance of the stripes. As shown in Figs. 1 and 2 (A and B), the MSK is likely to cover the entire cytoplasmic surface of the upper cell membrane except for the places where CCPs and caveolae are present in both NRK and FRSK cells. Such a notion of the complete coverage of the cytoplasmic surface of the plasma membrane by actin filaments might have existed for >30 yr in a part of the EM community (Byers and Porter, 1977; for review see Sheetz et al., 2006), but the data specifically indicating that the actin filaments of the MSK may cover the entire cell membrane has not been presented in the literature, as done here, nor shared in the cell biology community. The EM observations shown in this study are consistent with the MSK fence and anchored transmembrane protein picket models, in which the entire plasma membrane except for the specific membrane domains is partitioned into many small compartments with regard to lateral diffusion of the molecules incorporated in the plasma membrane.

The MSK predominantly consists of actin filaments: immunogold labeling of actin and actin-binding proteins

To further examine whether the MSK is predominantly composed of actin filaments (and partly because the 5.5-nm periodicity of the banding pattern is somewhat difficult to discern in some of the filaments), we examined it using an indirect immunolabeling method with 5-nm-diameter colloidal gold particles (see Materials and methods; Fig. 3). On the filaments with striped patterns, the enlarged images (Fig. 3, B and C) show the presence of many colloidal gold actin probes, which appear as distinct white spots surrounded by somewhat blurred white halos, reflecting the platinum shadow over the antibody molecules attached to the gold particle. The electron micrographs in Fig. 3 revealed that almost all of the colloidal gold probes are bound to the filaments located on the cytoplasmic surface (yellow dots). Therefore, it is concluded that actin is the main constituent molecule of the MSK.

Electron tomography of the undercoat structure on the cytoplasmic surface of the plasma membrane

The 3D structure of the undercoat within 100–134 nm from the cytoplasmic surface of the plasma membrane, which includes CCPs, caveolae, and the actin-based MSK, was reconstructed using electron tomography for the platinum-replicated samples. Based on the 97–141 tilt images acquired in the range of ±48–70° every 1° step for a single EM view field, 100–121 sliced images of every 0.85–1.34 nm perpendicular to the z axis (parallel to the image obtained at 0° of the tilt angle) were calculated by a computer (long wavelength [≥~500 nm] undulations of the cell membrane were corrected by the 3D reconstruction software IMOD). The 3D image was reconstructed based on these serial thin slices. Representative images obtained for an EM view field are shown in Video 1 (131 tilt images; an anaglyph produced from images taken at ±12° is shown in Fig. 4 A) and Video 2 (showing the 3D image by rotating the 3D reconstructed undercoat structure; a typical view is shown in Fig. 4 B; videos are available at http://www.jcb.org/cgi/content/full/jcb.200606007/DC1). Throughout the present research, this protocol was used to obtain 3D images.

In these images, because of their 3D representation, it is especially clear that the MSK, which is mostly composed of actin filaments, generally spreads along the membrane, covering almost the entire cytoplasmic surface of the upper membrane except for the places with caveolae and CCPs. In addition,

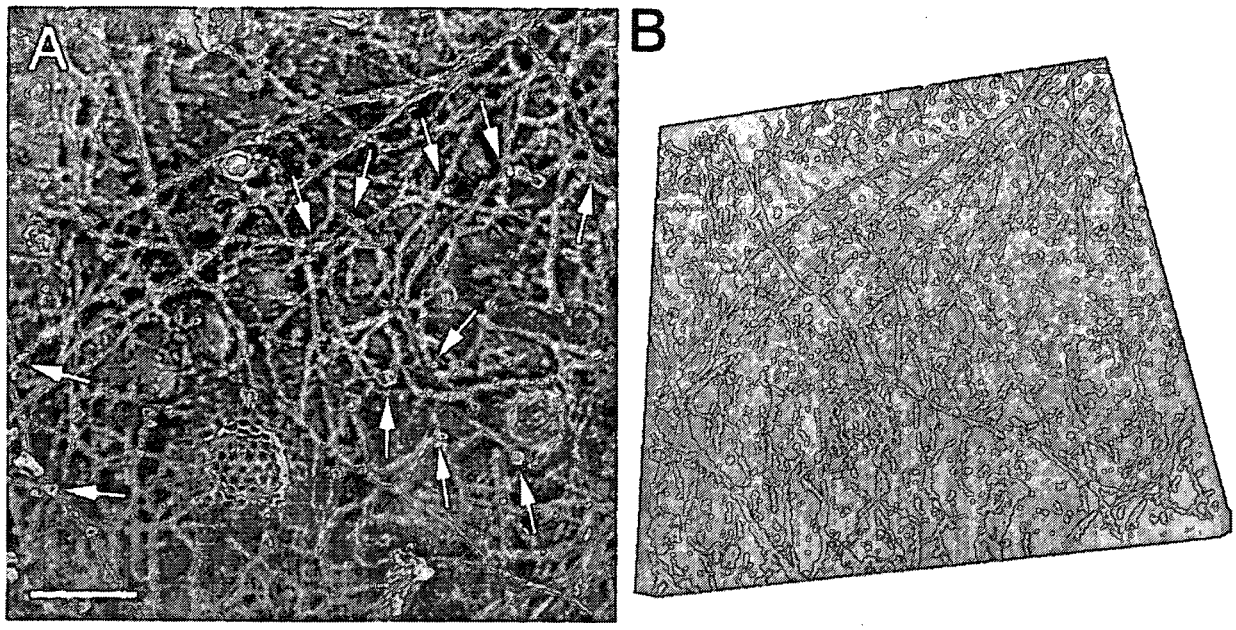

Figure 4. **Stereo electron micrographs and 3D reconstructed images of the undercoat structure, CCPs, and caveolae in NRK cells.** (A) An EM anaglyph of the undercoat structure generated at ±12° of the tilt angle among the 131 tilt images (acquired in the range of ±65° with 1° steps). Use view glasses for the 3D structure (left = red). See Video 1 for all 131 of the tilt images. Arrows indicate actin filaments protruding from the membrane cytoplasmic surface toward the cytoplasm. The arrows point to the places where the protruding actin filaments intersect with the MSK meshwork located close to the membrane. (B) The 3D undercoat structure reconstructed from the tilt images shown in Video 1. See Video 2, where the 3D structure is rotated (available at http://www.jcb.org/cgi/content/full/jcb.200606007/DC1). Bar, 100 nm.

CCPs and caveolae are very closely associated with the actin filaments in the MSK, as seen in these images and also in Figs. 2 (A and B) and 3. These results are consistent with Rothberg et al. (1992), Fujimoto et al. (2000), and Parton (2003), but in NRK cells studied here, many more actin filaments were found to be associated with each CCP or caveola. Furthermore, 92 and 93% of CCPs and caveolae (n = 200) were bound by the actin filaments. These results are consistent with the requirement of filamentous actin for CCP internalization (Qualmann et al., 2000; Merrifield et al., 2002).

Many short, thin filaments protrude toward the cytoplasm, mostly perpendicularly, from the membrane surface (they were short probably because they were broken at the time of the membrane rip off; Fig. 4 A, arrows). Note that these perpendicular filaments are almost always connected to the MSK network lying on the cytoplasmic surface (see the tips of the arrows; Fig. 4 A). Thus, the part of the MSK that is located on the cytoplasmic surface is connected three dimensionally to the cytoskeleton. Together, they will provide mechanical support for the membrane and the force for deforming the membrane.

3D reconstruction of the MSK structure

The part of the actin-based MSK that is in contact with the cytoplasmic surface of the cell membrane has been proposed to partition the cell membrane into 30–230-nm compartments by the fence and picket effect (Edidin et al., 1991; Kusumi and Sako, 1996; Kusumi et al., 2005). If these fence and picket models are correct, the distribution of the mesh size of the MSK on the cytoplasmic surface of the plasma membrane would be practically the same as that of the compartment size determined by diffusion measurements of membrane molecules. To carry out this examination, the 3D reconstruction of MSK by electron tomography provides a unique opportunity because the obtained images provide quantitative data on how far the individual filaments are located from the membrane surface.

In Fig. 5 A, a typical MSK structure quantitatively analyzed in this study is shown in an anaglyph, and its 8.5-nm–thick sections (created by superimposing 10 0.85-nm sections) of the MSK of an NRK cell, starting from the cytoplasmic side toward the membrane, are shown (Fig. 5 B; a series of the original tilt images is shown in Video 3, and a series of sliced images of every 0.85 nm is shown in Video 4, available at http://www.jcb.org/cgi/content/full/jcb.200606007/DC1). The actin-based MSK is visible on image sections 81–110. Individual actin filaments, forming a network as well as bundles, can be identified. Given the high density of the actin filament meshwork, which is much smaller than the optical resolution, conventional fluorescence microscopy will be unable to visualize the MSK meshwork and can visualize only the bundles of actin filaments.

Interface structure of MSK on the cytoplasmic surface of the plasma membrane

The filaments of the MSK that are directly associated with the cytoplasmic surface of the plasma membrane and may be involved in partitioning the plasma membrane were systematically determined. Out of the stack of 121 image slices taken every 0.85 nm from the cytoplasmic surface (~100-nm thick altogether),

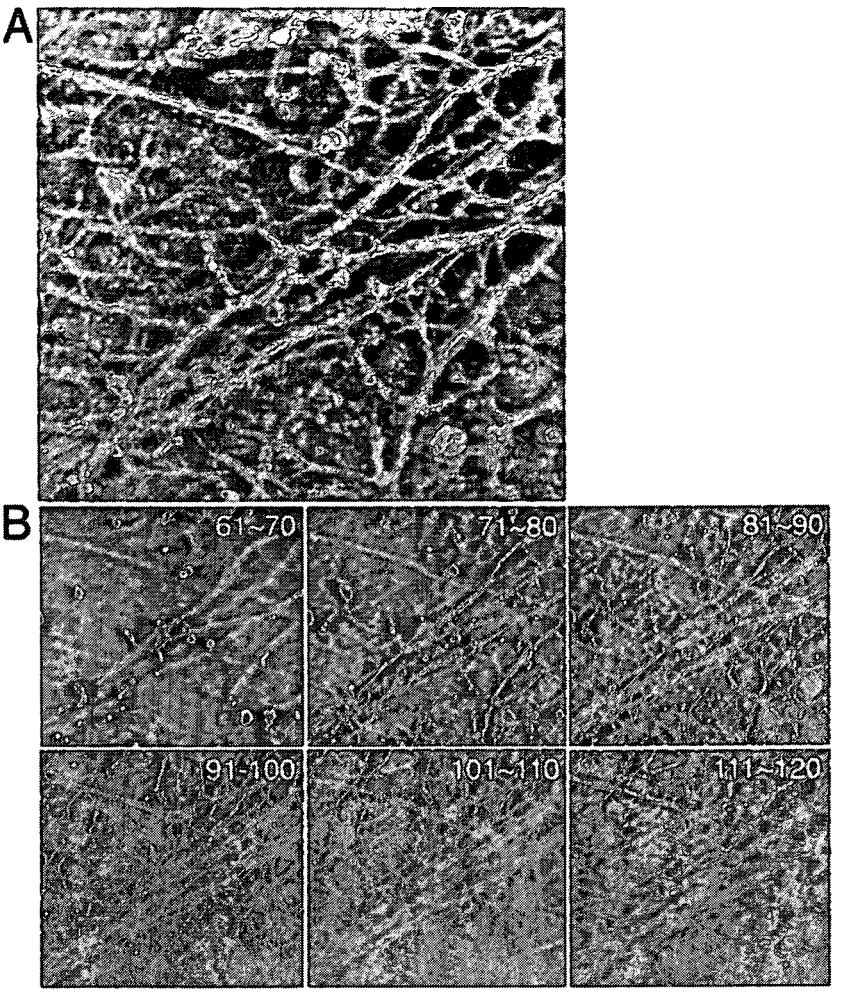

Figure 5. **A series of sliced images of the actin MSK on the plasma membrane cytoplasmic surface of an NRK cell.** (A) A typical actin MSK structure used for analysis of the mesh size on the cytoplasmic surface of the plasma membrane using computed tomography. An anaglyph of the undercoat structure generated at ±12° of the tilt angle among the 97 tilt images (acquired in the range of ±48° with 1° steps). See Video 3 for all 97 of the tilt images. (B) 10 consecutive sections, each 0.85-nm thick, are superimposed, and six of these superimposed images, which represent 60 image sections out of 121 image sections, are shown from the cytoplasmic side toward the plasma membrane side. The numbers here indicate the number of slices counted from the cytoplasmic side. The actin-based MSK near the cytoplasmic surface of the plasma membrane is visible on images 81–110. All 121 of the sliced images of every 0.85 nm are shown in Video 4 (available at http://www.jcb.org/cgi/content/full/jcb.200606007/DC1).

16 consecutive image slices from the membrane surface (~13.6-nm thick altogether) were used for this analysis (Fig. 6, A and B).

In Fig. 6 A (four images on the right) and Fig. 6 B (the second to fourth images), the boxed areas in the left-most images were expanded, and the sections of every 1.7 nm (superposition of two 0.85-nm–thick slices; 330 × 330 nm) are displayed between 0 and 11.9 nm. Using these sections, the filaments that are closely associated with the cytoplasmic surface of the cell membrane were determined. Because the thickness (width in the image) of the actin filament after platinum shadowing is between 9 and 11 nm (consistent with Heuser, 1983) and the thickness of the platinum replica is ≤2 nm (consistent with Heuser, 1983 and Moritz et al., 2000), the height of the actin filament that is associated with the membrane will be 7–9 nm (because the height is given by the actin thickness and one replica thickness, whereas the width in the image is determined by the actin thickness plus two replica thicknesses), with 8 nm being a reasonable estimate. In the series of electron tomography sections shown in Fig. 6 (A and B), the existence of three major classes of filaments with regard to the distance from the membrane surface can be discerned (for details of this analysis, see Materials and methods).

The first class of filaments is distinct in computer-reconstructed sections close to the cytoplasmic surface of the plasma membrane, even in the first ~0–1.7-nm section (because the contrast is reversed in these micrographs, they look more lucent or white), but fade out of the reconstructions 8–10 nm away from the membrane surface (for details, see Materials and methods). These filaments are drawn in green in Fig. 6 C. We interpret that these filaments are in true contact with the plasma membrane (the gap between the filament and the inner membrane surface is <0.85 nm) because they can be seen clearly even in the first 0.85-nm section. These filaments are likely to be the significant ones for generating membrane corrals.

The second class of filaments also looks clear in sections very close to the membrane surface but does not fade out until ~14 nm away from it. We interpret that these may be the actin filaments that had platinum coatings all around their surfaces because they stood off the surface somewhat, which slightly exaggerated their thickness and made them appear as though they were in contact with the plasma membrane when

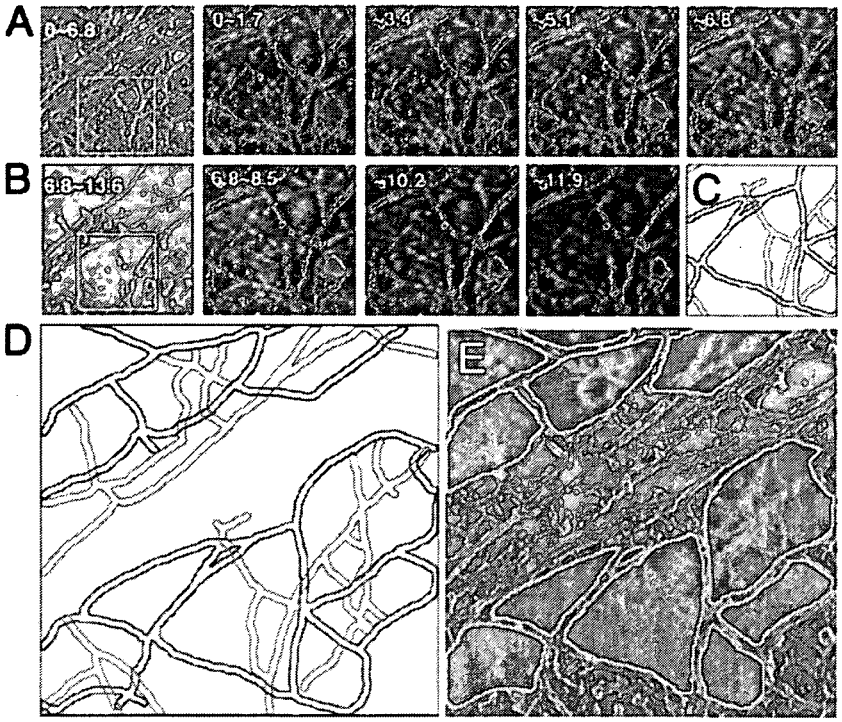

Figure 6. **The method for determining the MSK mesh on the cytoplasmic surface of the plasma membrane, which possibly delimits the compartments of the plasma membrane, using the 3D reconstructed images of the MSK (an NRK cell).** (A and B) The images on the far left are the ~0–6.8- or ~6.8–13.6-nm sections, each of which is a stack of eight 0.85-nm sections of 670 × 670 nm. These are from a series of 121 image sections (0.85-nm thick) from the cytoplasmic surface after the tilt and long wavelength undulation of the cell surface were corrected. The boxed areas in A and B (330 × 330 nm) are expanded on the right of these image stacks, with a section thickness of 1.7 nm (two 0.85-nm sections are superimposed; 330 × 330 nm for each image). (C) The outline of each actin filament adjacent to the membrane surface (green, which could not be observed above 10.2 nm) and that of each actin filament that could be observed above 10.2 nm (red). The same view field and magnification as those for the thinner sections shown in A and B (330 × 330 nm). See Materials and methods for details. (D) The outline of actin filaments in a greater view field, which is the same as those in the thick sections (~0–6.8 and ~6.8–13.6 nm) in A and B (670 × 670 nm, expanded here). (E) The image of the ~0–6.8-nm sections (670 × 670 nm) superimposed by the image of areas surrounded by the filaments outlined in green in D (green areas with yellow outlines). According to the fence and picket models, these areas are likely to be the compartments where membrane molecules are temporarily confined.

in fact they probably were not quite in direct contact. We did not consider these filaments to be close enough to generate membrane corrals.

The third class of filaments is not apparent in sections closest to the plasma membrane but becomes clear some distance away from it (>2–4 nm) and also does not fade out until ~14 nm. We interpret these as being filaments that definitely do not contact the plasma membrane directly and, thus, should not contribute to forming corrals. The second and third classes of filaments are drawn in red in Fig. 6 C.

Therefore, we considered that only the first class of filaments (those drawn in green in Fig. 6, C and D) forms the MSK fences and pickets, and the area surrounded by these filaments is colored green in the 0–6.8-nm section shown in Fig. 6 E. Note that areas are excluded from this analysis in which bundles of actin filaments are present (e.g., the structure crossing diagonally from the bottom left to the top right in Fig. 5), actin filaments are too crowded to be individually discerned, an actin filament is terminated in the middle of a domain (domains that contain a loose end of an actin filament), or CCPs, caveolae, and the smooth surface membrane invaginations are present (the white regions in Fig. 7 C).

Comparison of the MSK mesh size on the plasma membrane determined by electron tomography with the compartment size for the diffusion of membrane molecules

Similar determination of the MSK meshwork was performed for FRSK cells. Representative meshes of the MSK are shown in Fig. 7 (for an FRSK cell, colored to aid in visualization). We performed such analyses for 10 representative stacks of image sections (1,290 × 1,290-nm plane) each for NRK cells and FRSK cells (eight different cell membrane sheets for each cell type) and identified 76 and 1,300 areas bounded by the MSK meshwork, respectively (excluding the regions occupied by stress fibers and other membrane undercoat structures such as CCPs and caveolae; about the same total membrane areas were examined for each cell type, and, thus, the difference in the number of identified areas represents the difference in the area size between these two cell lines). The 2D area size for each domain was measured by Amira software. The distributions of the square root of the area size (the side length, assuming a square shape for the area) for NRK (Fig. 8, pink open bars) and FRSK (blue open bars) cells are shown in Fig. 8. The median values of the area and its square root are 3.9×10^4 nm^2 and 200 nm, respectively, for NRK cells and 2.7×10^3 nm^2 and 52 nm, respectively, for FRSK cells.

The size distributions of the compartments for the diffusion of membrane molecules were obtained for an unsaturated phospholipid, L-α-dioleoylphosphatidylethanolamine, by Fujiwara et al. (2002) and Murase et al. (2004) for NRK and FRSK cells, respectively. The distributions of the side lengths for NRK (Fig. 8, pink closed bars) and FRSK (blue closed bars) cells are shown in the histograms in Fig. 8. The median values of the compartment area and the side length are 4.3×10^4 nm^2 and 230 nm, respectively, for NRK cells and 2.1×10^3 nm^2 and 41 nm, respectively, for FRSK cells (Murase et al., 2004).